

Annual Report 2020

Laboratory of Environmental Chemistry

On the cover page:

The last two hot summers destroyed a glacier archive in the Swiss Alps.

Top – left to right: The 2020 Grand Combin ice core drilling team (without hygienic masks – the team worked isolated on the glacier, forming the Grand Combin “bubble”). View from southeast to the Corbassière glacier on Grand Combin, Switzerland, and the drilling camp in the saddle, where two ice cores were collected in 2018 and 2020.

Bottom – left to right: Sampling of the 2020 ice core in the cold room of the Paul Scherrer Institute. Thick ice lenses from refrozen meltwater are visible. While records of water stable isotopes ($\delta^{18}\text{O}$) agree well between the 2018 and 2020 cores, intense melt-water induced depletion of selected major ions (such as sulfate) was observed in the 2020 core.

Please see reports on p. 24 and 25.

PAUL SCHERRER INSTITUT



Annual Report 2020

Laboratory of Environmental Chemistry

Editors

M. Schwikowski, M. Ammann

Paul Scherrer Institut

Laboratory of Environmental Chemistry

Forschungsstrasse 111

5232 Villigen PSI

Switzerland

Phone +41 56 310 25 05

www.psi.ch/luc

Reports are available: www.psi.ch/luc/annual-reports



TABLE OF CONTENT

Editorial.....	1
Surface Chemistry	
X-RAY SPECTROMICROSCOPIC INVESTIGATION OF ICE FORMING PARTICLES P. A. Alpert, A. Boucly, S. Yang, H. Yang, M. Ammann, Z. Luo, C. Padeste, S. Finizio, B. Watts.....	3
A STATE-OF-THE-ART ENVIRONMENTAL SAMPLE HOLDER FOR SLS T. Bartels-Rausch, A. Laso, Y. Manoharan, J. Gabathuler, H. Yang, A. Boucly, L. Artiglia, M. Ammann.....	4
PHOTON FLUX MEASUREMENT AT ISS J. P. Gabathuler, H. Yang, L. Artiglia, M. Ammann, T. Bartels-Rausch.....	5
THE PROBING DEPTH IN ELECTRON SPECTROSCOPY BY MONTE CARLO J. P. Gabathuler, P. A. Alpert, M. Ammann, T. Bartels-Rausch.....	6
VERTICAL CHARACTERISTICS OF PARTICLES AT A COSTAL REGION B. Wang, L. Yang, T. Zhang, P. A. Alpert, M. Ammann, J. Dou, U. Krieger.....	7
LIQUID-LIQUID PHASE SEPARATED ORGANIC AEROSOL IN URBAN HAZE S. Yang, F. Duan, K. He, P. A. Alpert, M. Ammann.....	8
MISCIBILITY OF DIFFERENT TYPES OF ORGANIC AEROSOL F. Mahrt, Y. Huang, E. Newman, M. Ammann, A. K. Bertram.....	9
SPONTANEOUS REDOX REACTION ON SOLVATING INORGANIC AEROSOL X. Kong, I. Gladich, D. Gastarede, E Thomson, A. Boucly, L. Artiglia, M. Ammann, J. Pettersson.....	10
IN SITU XPS AND XAS CHARACTERIZATION OF IRON IN AQUEOUS SOLUTIONS L. Artiglia, I. Gladich, S. Chen, H. Yang, A. Boucly, J. A. van Bokhoven, M. Ammann.....	11
A LINE DRAWN FOR PHOTOCHEMICAL REACTIONS IN AEROSOL PARTICLES P. A. Alpert, K. Kilchhofer, M. Ammann.....	12
CONSTRAINING PHOTOCHEMISTRY IN ORGANIC AEROSOL WITH CO ₂ K. Kilchhofer, L. Iezzi, T. Berkemeier, S. Bachmann, P. A. Alpert, M. Ammann.....	13
IRON(III)-CITRATE PHOTOLYSIS INDUCED CONVERSION OF NO ₂ L. Iezzi, K. Kilchhofer, M. Ammann.....	14
PYRUVIC ACID KETO/GEM-DIOL EQUILIBRIUM: EXPERIMENT AND THEORY A. Boucly, L. Artiglia, H. Yang, A. Roose, A. S. P. Gomes, V. Vallet, M. Masella, M. Ammann.....	15
SURFACE PROPERTIES OF AQUEOUS RESORCINOL SOLUTIONS H. Yang, L. Artiglia, A. Boucly, M. Ammann.....	16
TOWARDS FAST AND ULTRAFAST IODINE CHEMISTRY IN THE LIQUID PHASE Y. Uemura, M. Ammann, T. Lind, D. J. Suckow, M. Nachtegaal, C. Milne, P. Johnson.....	17
INVESTIGATION OF AQUEOUS IODINE CHEMISTRY IN THE TROPOSPHERE A. Roose, M. Ammann, M. Reza, H. Finkenzeller, R. Volkamer, C. Toubin, V. Vallet, A. Tilgner, E. Hoffmann, H. Herrmann.....	18
IS IODIDE A SINK FOR OZONE IN THE STRATOSPHERE? S. Gysin, L. Iezzi, A. Roose, M. Reza, H. Finkenzeller, R. Volkamer, T. Peter, M. Ammann.....	19
PHOTOEMISSION OF AQUEOUS IODINE SPECIES: THEORY AND EXPERIMENT A. Roose, A. Boucly, H. Yang, L. Iezzi, C. Toubin, V. Vallet, L. Halbert, A. S. P. Gomes, R. Opoku, M. Ammann, L. Artiglia.....	20

Analytical Chemistry

ALPINE ICE CORES – REPRESENTATIVE ARCHIVES OF PAST AIR POLLUTION A. Eichler, T. M. Jenk, M. Legrand, S. Preunkert, M. Schwikowski	21
MODELING exSO_4^{2-} CONCENTRATIONS IN PRECIPITATION AT 4 ALPINE SITES C. Andersson, M. Engardt, T. M. Jenk, M. Legrand, T. Olenius, S. Preunkert, M. Schwikowski, A. Eichler	22
THE ICE MEMORY PROGRAM M. Schwikowski, C. Barbante, J. Chappellaz, P. Ginot, A.-C. Ohlmann	23
ICE CORE DRILLING ON GRAND COMBIN IN TIMES OF A WARMING CLIMATE T. M. Jenk, J. Gabrieli, F. de Blasi, F. Dallo, C. Barbante, R. Lodi, P. Conz, R. Selvatico, T. Singer, M. Schwikowski	24
MELTING INFLUENCED SIGNAL PRESERVATION AT GRAND COMBIN GLACIER C. J. Huber, A. Eichler, S. Brüttsch, T. M. Jenk, J. Gabrieli, C. Barbante, M. Schwikowski	25
CARBONACEOUS AEROSOL RECORD OF TWO ALPINE ICE CORES T. Singer, L. Fang, T. M. Jenk, M. Schwikowski	26
METHOD FOR DETERMINING ORGANIC FIRE TRACERS IN ICE CORES F. Burgay, D. Salionov, A. Eichler, T. Singer, C. J. Huber, S. Bjelic, M. Schwikowski	27
ANALYSIS OF FIRE TRACERS IN ICE CORES J. Stoll, M. Schwikowski, F. Burgay, A. Eichler, D. Salionov, S. Bjelic	28
THE DIFFICULTY OF ALIQUOTING ICE CORE SAMPLES T. S. Münster, T. M. Jenk, C. J. Huber, A. Eichler, P. Nalivaika, M. Schwikowski	29
ALBEDO REDUCTION AND ENHANCED MELT RATES OF OLIVARES GLACIERS M. Barandun, A. Rivera, C. Bravo, B. Grobety, L. Fang, S. Köchli, T. S. Münster, K. Naegeli, S. Cisternas, M. Schwikowski	30
CROSS DATING OF TWO BELUKHA ICE CORES V. Wilson, A. Eichler, S. Brüttsch, P. Nalivaika, T. Singer, T. Papina, M. Schwikowski	31
CROSS-DATED ICE CORE RECORDS FROM THE TSAMBAGARAV GLACIER P. Nalivaika, L. Marti, T. Singer, S. Brüttsch, T. M. Jenk, T. Papina, M. Schwikowski, A. Eichler	32
FIRST Pb RECORD FROM THE TSAMBAGARAV ICE CORE P. Nalivaika, T. S. Münster, M. Schwikowski, T. Papina, T. M. Jenk, A. Eichler	33
List of Publications	34
Affiliation Index	36

EDITORIAL

For our Laboratory of Environmental Chemistry (LUC) the year 2020 was as challenging as for everybody else. Due to COVID-19 measures, access to PSI was substantially reduced, which was especially demanding for LUC with our strong focus on experimental work. In addition, we faced a major turnover in our team with 18 new PhD/MSc students and Postdocs starting in 2019 and 2020. All of them wanted to be trained and work in the lab to start with their research projects, which was only possible to a limited degree. I would therefore like to take this opportunity to thank all LUC members for their patience, support and solidarity that enabled us to keep our lab running as best as possible under the adverse circumstances!

The outcome of this effort is nevertheless exciting science, cumulating in overall 27 papers in peer-reviewed scientific journals. One of the topics of the Surface Chemistry Group was multiphase chemistry of halides in the atmosphere with emphasis on iodine and its role in the ozone budget. Further, the group pioneered technical developments for in-situ XPS and X-ray microspectroscopy at SLS. For instance, they designed a unique cryo-holder for surface science studies at elevated relative humidity. They also supported the development of a multipurpose microreactor system (MIMiX) to observe physical and chemical changes in aerosol particles in-situ under environmental conditions, which can now be used by collaborators at other synchrotron facilities.

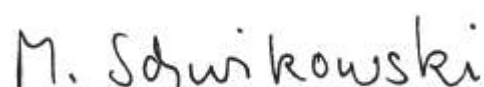
A major activity of the Analytical Chemistry Group was cross-dating different ice cores from the same glacier, revealing excellent agreement between the glacio-chemical records. After several postponements due to unfavourable weather conditions and COVID-19 restrictions, members of the group conducted an ice core

drilling campaign on the summit plateau of Corbassière glacier, in the saddle of Grand Combin, Switzerland. This was an expedition in collaboration with our colleagues from University Ca' Foscari in Venice, funded by the Italian Ministry of Education, University and Research within the frame of ICE MEMORY.

The international ICE MEMORY program aims at collecting heritage ice cores from the world's key endangered glaciers to store them under safe conditions and international governance in Antarctica for future generations of scientists. Starting in 2015 as a Franco-Italian initiative, a major step forward was the creation of the international ICE MEMORY FOUNDATION, which gives the program a legal status. PSI is one of the seven founding members and the agreement was signed on 18 January 2021 during a virtual ceremony. This is included here, because the preparatory work happened in 2020.

On 2 June 2020 Ling Fang successfully defended her PhD at the University of Bern. This was the first time that a student from our lab defended online and Ling delivered a great performance. Congratulations! Similarly, most of our teaching activities and exams at the ETHZ and University of Bern were conducted online or in hybrid mode – a new experience for everybody.

In all my previous editorials, I mentioned our LUC excursions and other social activities, but for 2020 there is unfortunately not much to say. I deeply hope this will change for the 2021 report.



Margit Schwikowski

X-RAY SPECTROMICROSCOPIC INVESTIGATION OF ICE FORMING PARTICLES

P. A. Alpert (PSI), A. Boucly (PSI LEC & LUC), S. Yang (THU & PSI), H. Yang (PSI & ETHZ), M. Ammann (PSI), Z. Luo (PSI LMX), C. Padeste (PSI LMN), S. Finizio, B. Watts (PSI LSC)

We approach the nanometer scale for observing single particles responsible for forming ice using a new ice nucleation X-ray microscope cell INXCell, and we quantify the rate at which ice forms.

Organic aerosol components are among the most common in atmospheric particles and well-recognized as important ice nucleating particles [1]. Ice formation is important for snow, sleet and hail precipitation, but also for rain, i.e., about two-thirds of rain begins as ice crystals nucleated from aerosol particles [2]. Ice forms from ice-like water molecular clusters, also known as ice embryos, which is one of the many reasons why ice formation is one of the most uncertain atmospheric phenomena to predict and fully understand. To address the difficulty in chemical and physical characterization of ice nucleating particles, we developed the INXCell to have 3 main advantages, chemical selectivity, high spatial resolution and in situ capability. The INXCell can image a particles' chemical composition with a spatial resolution of 35 nm in an atmospheric chamber while an ice nucleation experiment is ongoing. The chemical composition, in particular, is determined from a near-edge X-ray absorption fine structure (NEXAFS) spectrum, which determines the absorption of X-rays as a function of X-ray energy across the entire image. We used iron containing nano-particles, ferrihydrite, which were coated and uncoated with citric acid to mimic atmospheric mineral-type aerosol particles with and without organic coatings. Ferrihydrite is an amorphous iron oxyhydroxide compound that is ubiquitous in nature and recently found to be abundant in urban air masses and combustion sources [3]. Citric acid is also a well-known proxy in terms of composition and viscosity for atmospheric oxidized organic aerosol particles [4].

Fig. 1 (A-D) shows X-ray images taken after ice nucleation occurred and during ice crystal sublimation. The residual and non-residual particles probed using NEXAFS spectroscopy pertaining to iron (E) and carbon (F) of one residual particle and one non-ice nucleating particle are shown. The spectra are highly similar, meaning that both particles have a spectroscopically similar iron and organic composition, which are ferrihydrite and citric acid, respectively. Although this was expected, it does imply that chemically distinctive ice active features were not observed on our spatial scales and for iron or carbon. This finding is counter to the hypothesis that ice nucleation occurs on ice active sites. Alternatively, we find that ice nucleation may have occurred on one particle by chance, i.e. ice nucleation occurred stochastically and in line with nucleation theory. This has implications for how ice formation is predicted [5], meaning that stochastic modelling should be implemented for better prediction.

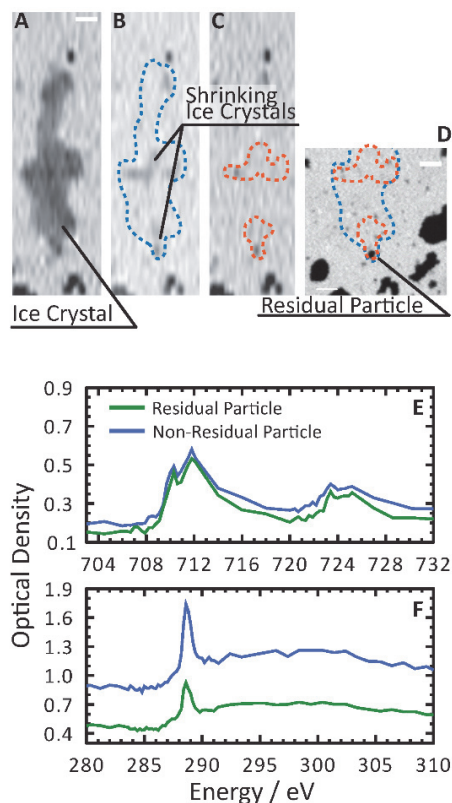


Fig. 1: Ice nucleation and spectroscopic identification of ferrihydrite particles coated with citric acid. A sequence of X-ray images (A-C) show the last instances of a sublimating ice crystal. The coarse resolution was necessary to quickly image the shrinking crystal. The blue and orange outline indicate the crystal boundaries on (A) and (C), respectively. The X-ray image in (D) shows residual and organic rich particles across the sample. The scale bar in (A) and (D) indicate the same length at 2 μm . NEXAFS spectra were acquired first at the carbon K-edge (F) and then the iron L-edge (E) of a residual particle and a non-ice nucleating particle.

We acknowledge funding from the European Union's Horizon 2020 research and innovation program under the Marie Skłodowska-Curie grant agreement (701647).

- [1] D. A. Knopf, P. A. Alpert and B. Wang, *ACS Earth Space Chem.*, **2**, 168-202 (2018).
- [2] K. M. Lau and H. T. Wu, *Geophys. Res. Lett.*, **30**, 24, 2290 (2003).
- [3] A. Ito et al., *Sci. Adv.*, **118**, 5 (2019).
- [4] J. Reid et al., *Nat. Comm.*, **9**, 15002 (2018).
- [5] P. A. Alpert and D. A. Knopf, *Atmos. Chem. Phys.*, **16**, 2083-2107 (2016).

A STATE-OF-THE-ART ENVIRONMENTAL SAMPLE HOLDER FOR SLS

T. Bartels-Rausch, A. Laso (PSI), Y. Manoharan, J. Gabathuler, H. Yang (PSI & ETHZ), A. Boucly (PSI LEC & LUC), L. Artiglia (PSI LSK & LUC), M. Ammann (PSI)

Temperature is a key factor in atmospheric chemistry. Here, we present a new sample holder that allows to control and monitor the temperature of samples for X-ray excited electron spectroscopy work at SLS with improved precision.

We have recently investigated interfacial phase changes of sea-salt aerosol by means of X-ray excited electron spectroscopy [1]. Temperature calibration was of paramount importance in this study identifying supercooled liquid on ice surfaces at 240 K, well below the freezing point. This is of environmental relevance, because chemical multiphase reactions in aerosol generally proceed faster as long as the particles are not frozen and the precise freezing temperature is still under debate.

These experiments have been done with a sample holder where temperatures down to 160 K can be reached by cooling with a flow of cold gas [2]. Figure 1 shows a sketch of an improved version of the sample holder.

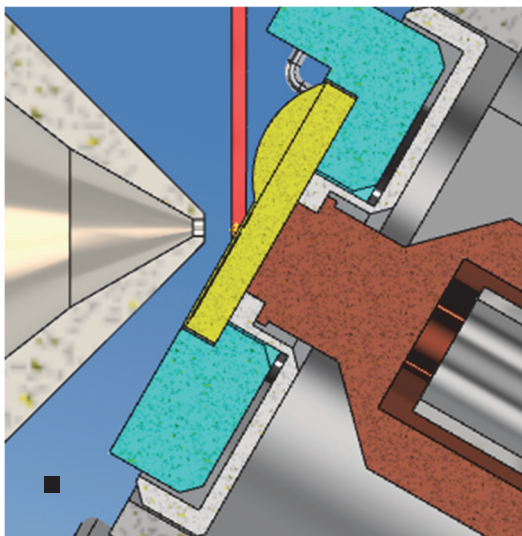


Fig. 1: The cryo-sample holder consisting of a sample plate (yellow) and of a cold finger (red) temperature regulated with a stream of cooled gas. Also shown is the electron acceptance cone of the electron analyzer (grey) and the X-ray beam (red) hitting the sample. The sample is directly placed on a gold covered thermocouple (yellow). The black bar denotes 500 μm .

The key feature of this improved version is that the sample is located directly on a gold covered thermocouple used to monitor the temperature (Fig. 1). This leads to a very direct measure of sample temperature with a mean off-set for 6 samples of 0.07 K as compared to up to 6 K with the previous sample holder. The sample plate can

be removed to prepare samples off-line, before beam-time starts.

Great emphasis in the development was placed on thermally isolating the gold coated thermocouple from the sample holder. Figure 2 shows an ice sample clearly constrained to the gold coated sample area and not forming on the outer parts of the sample holder. Such a well-defined cooled area has advantages when dosing trace gases to the sample and also of a minimized temperature gradient across the sample area.

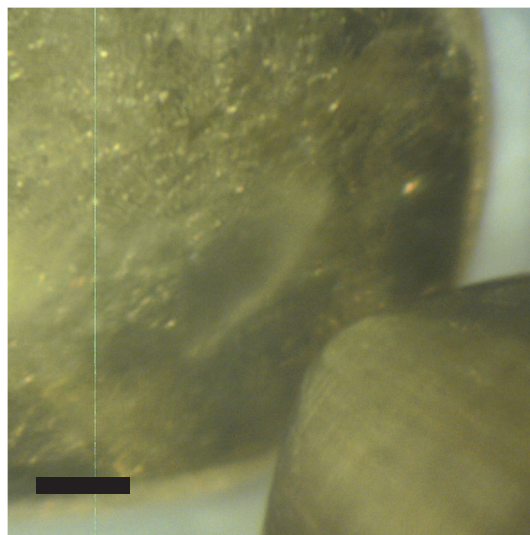


Fig. 2: Ice sample grown on the gold coated thermocouple. The outer parts (white) made of glass-ceramic appear ice free. The electron acceptance cone of the analyzer is shown in the front of the picture. The black bar denotes 500 μm .

The detailed characterisation and optimisation of the new sample holder during four beamtimes in 2020 further showed supreme cooling rates and great improvement in sample purity. Ice samples, for example, were free of adventitious carbon that is often present in near ambient pressure X-ray excited electron spectroscopy.

We acknowledge funding from the Swiss National Science Foundation (Grant 178 962).

- [1] T. Bartels-Rausch et al., *The Cryosphere Discuss.*, 1-26 (2020).
- [2] F. Orlando et al., *Top. Catal.*, **59**, 591-604 (2016).

PHOTON FLUX MEASUREMENT AT ISS

J. P. Gabathuler, H. Yang, (PSI & ETHZ), L. Artiglia (PSI LSK & LUC), M. Ammann, T. Bartels-Rausch (PSI)

The In-Situ Spectroscopy (ISS) beamline uses a spherical grating monochromator to select the photon energy. Such gratings also transmit a fraction of higher order light. We present here flux measurements of the 1st order and higher order contribution.

The term “higher order light” designates photons whose energies are an integer multiple of the fundamental (set by the monochromator). We usually talk about 2nd order and 3rd order light, the following orders having too weak intensity. At ISS, experiments are performed with the 1st order, while the photon flux is typically assessed by a photodiode that measures the total beam intensity, thus systematically overestimating 1st order flux. Due to geometrical reasons, it is not feasible to mount a high order suppressor at the ISS beamline. More precisely, in the photodiode, the total flux of photons generates a current I_0 according to the formula:

$$I_0 = \frac{h\nu \cdot flux}{3.6}$$

where $h\nu$ is the photon energy and 3.6 [W/A] is the quantum efficiency of the photodiode. From the formula, we obtain that 2nd (3rd) order light gives 2 (3) times more current per photon than the 1st order, respectively. Hence, even a small fraction of higher order light can yield to a significant error in the photon flux measurement, which is a key calibration step for some experiments in surface characterization for environmental science and catalysis.

To disentangle the contribution of higher order light from the 1st order light in the diode measurement, we use X-ray photoelectron spectroscopy (XPS) to assess the photon flux. The photoemission spectrum is composed of peaks located at a kinetic energy $KE = h\nu - BE$, where BE is the binding energy of the core shell of interest. There will be as many peaks as there are orders of light in the beam, and the area of the peaks is proportional to the photon flux of the respective order.

In Fig. 1, we see that 2nd order light contribution is relevant below 700eV, while 3rd order contributes below 500eV. In addition, we can note that the 100 nm SiN_x window separating the high vacuum beamline from the few millibars of pressure in the experimental chamber strongly absorbs at the nitrogen edge (~398 eV). The transmittance then increases from 400 to 1000 eV and is almost fully transparent above 1000 eV. Consequently, 1st order light in the region from 400 to 700 eV is more absorbed than the 2nd order (from 800 to 1400 eV) and the window acts as an amplifier on the HO light fraction at such low excitation energies.

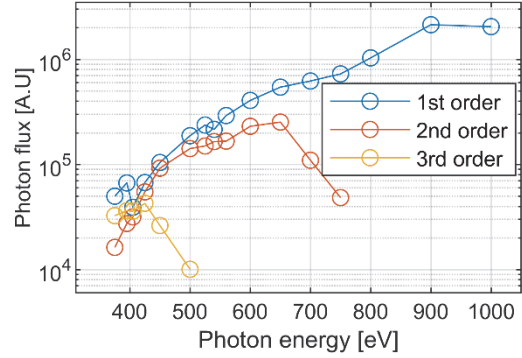


Fig. 1: Photon flux of the 1st, 2nd and 3rd order retrieved from Au4f photoemission peaks. Note the logarithmic scale.

Fig. 2 shows the relative contribution of higher order light to the total photon flux. These results are in line with the simulations shown in a publication describing ISS’ twin beamline, PolLux [1].

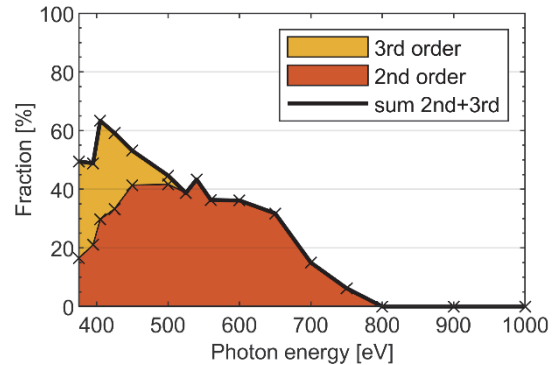


Fig. 2: Fraction of 2nd order light and 3rd order with respect to the total flux. The 1st order corresponds to the white area in the graph.

We nicely see in Fig. 2 a steep increase in 3rd order fraction as the 1st order is being absorbed at the nitrogen edge. A similar effect is visible at the oxygen edge (535eV), probably due to some oxygen contamination.

We acknowledge funding from the Swiss National Science Foundation (grant 178962).

- [1] U. Flechsig et al., AIP Conf Proc, **879**, 505-508 (2007).

THE PROBING DEPTH IN ELECTRON SPECTROSCOPY BY MONTE CARLO

J. P. Gabathuler (PSI & ETHZ), P. A. Alpert, M. Ammann, T. Bartels-Rausch (PSI)

Partial Electron-Yield X-ray Absorption Spectroscopy (PEY-XAS) is a powerful technique to study interfaces. However, the exact probing depth is a key uncertainty in PEY-XAS. A very simple Monte Carlo simulation gives quantitative answers.

In matter, an electron travels on average one inelastic mean free path (IMFP) of electrons in matter ($\lambda \approx 2.2$ nm) before it undergoes an inelastic scattering event, upon which it loses part of its kinetic energy (on average ~ 60 eV [1]). The electrons that scatter multiple times likely come from deeper in the sample being investigated [2]. Therefore, the electron kinetic energy that we can precisely measure in PEY-XAS contains depth information.

The Monte Carlo method is particularly well suited to understand the physics of inelastic scattering, and to find the relationship between the kinetic energy and probing depth. The simulation presented here generates 10^6 electrons with a kinetic energy spread between 450-500 eV and allows them to scatter until reaching the surface and escaping the sample. The key advantage of the simulation is the ability to retrieve the origin distribution of the electrons detected by the analyzer. Primary electrons, the ones that have not scattered, have an origin distribution that follows an exponential decay with depth. Secondary electrons, on the other hand, have a small probability to come from the surface, because they must scatter at least once. Fig. 1 shows such an origin distribution for electrons that escape the surface with a kinetic energy between 412 eV and 437 eV.

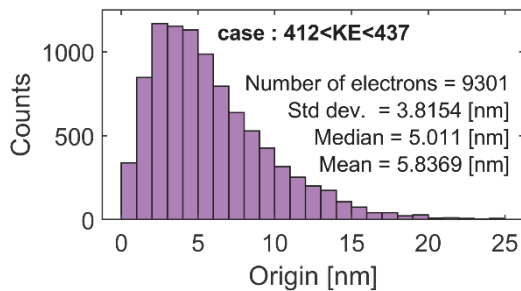


Fig. 1: Distribution of origin for a set of electrons that escaped the surface within the kinetic energy window 412-437 eV, simulated with the Monte Carlo algorithm.

Suppose now that we have a system composed of a layer A, of thickness D , sitting on top of a bulk B. The integration of the origin distribution from 0 to D allows to calculate the relative contribution of A to the total signal. In the case where electrons do not scatter, one can derive analytically:

$$\text{Signal A [\%]} = \int_0^D \frac{1}{\lambda} e^{-\frac{z}{\lambda}} dz = 1 - e^{-\frac{D}{\lambda}} \quad (1)$$

Fig. 2 shows the calibration curves that allow to convert the signal of A, as measured in PEY-XAS, into the thickness of the layer A. The simulation reproduces the analytical calculation (1) shown in Fig. 2 (black dashed line), and covers the kinetic energy windows where an analytical calculation is not trivial.

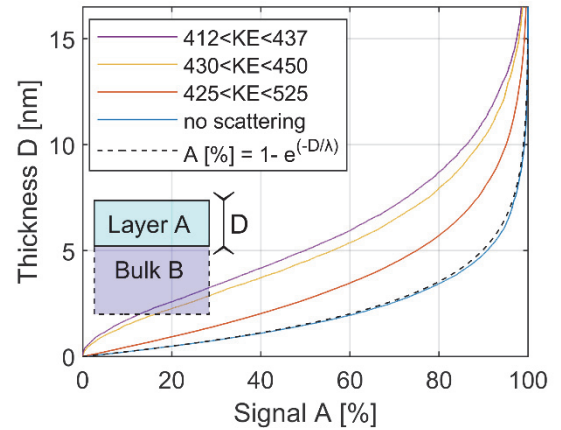


Fig. 2: Calibration curves to convert the signal A, derived from a PEY-XAS measurement and expressed in [%], into the thickness D of the layer A. Calculated from the simulated distributions of origin.

This shows that PEY-XAS can probe different depths by choosing varying kinetic energy window of the detected electrons. This technique has been successfully demonstrated on a SiO₂/Si sample [3] and could be used on ice surfaces to probe different regions of the interface. The gas phase associated with ice can also be simulated in order to disentangle the condensed phase scattering from the gas phase scattering.

We acknowledge funding from the Swiss National Science Foundation (grant 178962).

- [1] NIST Standard Reference Database
- [2] W. S. M. Werner, Surf. Interface Anal., **31**, 141-176 (2001).
- [3] N. Isomura et al., J. Appl. Phys., **122**, 025307 (2017).

VERTICAL CHARACTERISTICS OF PARTICLES AT A COSTAL REGION

B. Wang, L. Yang, T. Zhang (Xiamen Univ.), P. A. Alpert, M. Ammann (PSI), J. Dou, U. Krieger (ETHZ)

Aerosol composition and morphology at a coastal area in China was investigated using single particle X-ray spectromicroscopy and an unmanned aerial vehicle (UAV) to attain high resolution vertical profiles.

Atmospheric particle composition and morphology changes alter their ability to form clouds, to scatter light and thus, impact our environment and climate. We focus on the chemical and morphological characteristics of sea spray aerosol (SSA) particles, known to undergo acid displacement reactions liberating HCl, depleting sea salt, and increasing organic mass, when mixed with anthropogenic components in coastal areas [1]. There is limited understanding of how SSA composition and morphology changes during their residence in urban air.

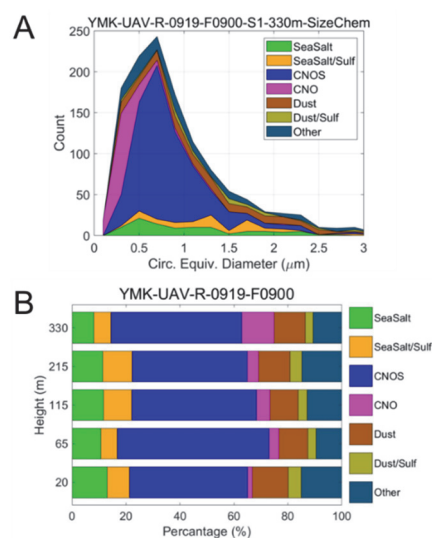


Fig. 1: (A) Size resolved chemical classification based on CCSEM/EDX analysis of particles at 330-meter height and (B) vertical distribution of each particle types in number percentage.

Here, we show a single particle analysis case study featuring vertical aerosol profiles obtained with an UAV system in Shenzhen, China, from 20 to 330 m in Sept. 2019 during morning hours. Size resolved elemental composition of tens of thousands of single particles were obtained from computer controlled scanning electron microscopy coupled to energy dispersive X-ray analysis (CCSEM/EDX) shown in Fig. 1. The aerosol population collected at 330-meter in the morning was dominated by sulfur-containing particles (CNOS), ~ 50% by number to the total population. Sea salts contributed less than 20% as shown in Fig. 1B, and decreased in abundance with height. Carbonaceous particles without sulfate increased in abundance with height in comparison. This indicates an exchange between ocean emission and anthropogenic emission during the

300 m transport, which we suspect may be SO₂ to sulfate conversion within individual sea spray particles.

An example of X-ray compositional mapping conducted on the same sample is shown in Fig. 2 along with NEXAFS spectra. The sea salt or sulfate indicated in cyan color were typically coated by organic matter indicated in green color in Fig. 2A dominated by the carboxyl (COOH) function and likely stemming from atmospheric oxidation processes or marine biogenic activity. NEXAFS spectra of two particles are shown in Fig. 2B, where the X-ray optical density is $-\ln I/I_0$, and I and I_0 are the transmitted and incident X-ray photon count through the particles as a function of X-ray energy. These particles contained carbon-carbon double bonding absorption features at 284.7 and 285.4 eV, indicative of quinone and soot-like compounds. Note, particle 1 was coated with more inorganic matter than particle 2, which was coated by organics by comparison. Quinones are known light absorbing compounds that initiate photochemical reactions, radical generation and cycling important for continual compositional change. An additional feature at 287.1 eV was observed and could be either quinone substituted carbonyl or hydroxyl functions. A previous study found that quinone concentration in aerosol particles was significantly higher when they were transported over coastal regions than over more continental areas [2]. We suspect that the presence of quinone compounds may be a unique feature of mixed anthropogenic and marine derived particle and formed in situ.

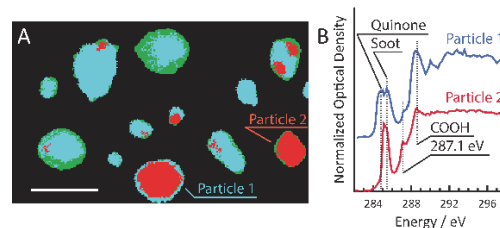


Fig. 2: (A) X-ray compositional mapping where the cyan, green and red color indicate areas of particles dominated by inorganic, carboxyl functions or carbon double bonding. (B) Carbon K-edge spectra for two different particles.

We acknowledge funding from the National Natural Science Foundation of China (Grant 41775133), the National Key Research and Development Program of China (Grant 2018YFC0213105) and the Swiss National Science Foundation (Grant 188662).

- [1] A. Laskin et al., *Annu. Rev. Anal. Chem.*, 9, 117-143 (2016).
- [2] M. Y. Chung et al., *Environ. Sci. Technol. Chem.*, 40, 4880-4886 (2006).

LIQUID-LIQUID PHASE SEPARATED ORGANIC AEROSOL IN URBAN HAZE

S. Yang, F. Duan, K. He (THU), P. A. Alpert, M. Ammann (PSI)

In situ X-ray microscopy demonstrates how aerosol particles from Beijing during winter haze undergo liquid-liquid phase separation (LLPS) at high relative humidity leading to core-shell chemical morphology.

Organic aerosol (OA) particles are frequently mixed with other components, namely inorganic material such as sulfate, nitrate and ammonium, organic compounds, metals, soot, and liquid water in the atmosphere. Meanwhile, it is well known that mixed inorganic and organic particles could undergo liquid-liquid phase separation (LLPS) [1]. LLPS has been observed in laboratory studies with bulk aerosol organic matter and surrogate particles [1, 2], but it has never been directly observed in single ambient aerosol particles. The physiochemical properties of particles, such as optical properties and chemical reactivity, can change when phase separation occurs compared to a well-mixed homogenous aerosol particle. Phase separation in single authentic atmospheric aerosol particles with chemically selective detection has remained unobserved until now.

We investigated the ability of ambient aerosol particles to phase separate in the PoLux environmental cell using scanning transmission X-ray microscopy coupled with near-edge X-ray absorption fine structure (STXM/NEXAFS) spectroscopy during in situ exposure to controlled temperature and relative humidity (RH). We imaged ambient particles collected in urban winter haze events (Beijing, China, with $PM_{2.5}$ mass concentration $> 150 \mu\text{g m}^{-3}$) at different RH levels to observe phase separation at a spatial resolution of $35 \times 35 \text{ nm}$ and with sensitivity to organic carbon (OC), inorganic (In) and soot or elemental carbon (EC) components.

Individual ambient aerosol particles were exposed to full hydration-dehydration cycles (dry - 60% - 97% - 80%) in the in-situ cell. One example of particles that took up water and changed their chemical morphology when RH increased is shown in Fig. 1. These images are colored to show which component is dominant, green for OC-rich, cyan for In-rich and red for EC-rich. These unique chemical morphological features are determined from an automated analysis based on similar NEXAFS features of various individual organic, inorganic and soot particles [3]. It is important to note that just because a particular color of a particle is e.g., OC-rich, does not necessarily mean that In and EC component are not present there. Only that OC is the dominant chemical composition in comparison to EC and In.

At RH = 97%, particles feature a large area of the In component indicative of aqueous solution due to water uptake (Fig. 1a). However, a thin layer of OC was still

present at RH = 97% at the perimeter of the particles indicating an OC-rich phase at the particle surface layers. As RH decreased to 81% (Fig. 1 b-d), the water-rich (In) cores shrank (less water present) while the OC-rich coatings increases in area, which we expect was due to the transfer of organic solutes into the organic phase.

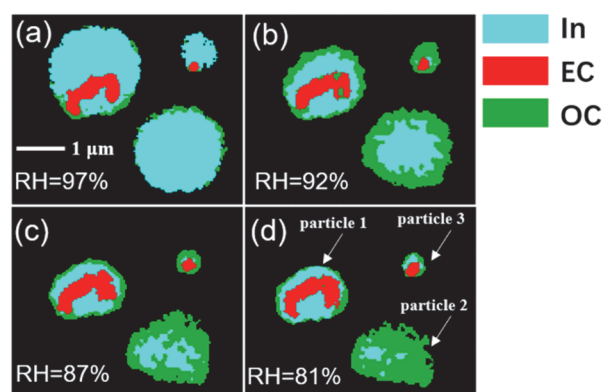


Fig. 1 (a)-(d): The false color images derived from STXM/NEXAFS data as a function of RH; it is obvious that the inorganic center is surrounded by a thick layer of organic coatings;

Fig. 1 shows direct evidence of LLPS for particles collected during Beijing haze. Our LLPS results and observations of changing particle morphology are beneficial to predicting hygroscopic growth, aqueous chemical kinetics, SOA formation mechanisms, aerosol optical properties and thus climate effects. They also give insights into the critical role of LLPS during multiphase reactions in urban haze formation, not only in the Northern China Plain, but also in regions with mixed organic-inorganic composition in particles characterized with high $PM_{2.5}$ mass concentrations worldwide.

We acknowledge funding from the National Science and Technology Program of China (grant 2017YFC0211601), the National Research Program for Key Issues in Air Pollution Control (DQGG0103).

- [1] R. E. O'Brien et al., *Environ. Sci. Technol.* **49**, 4995-5002 (2015).
- [2] Y. You et al., *Proc. Natl. Acad. Sci. U.S.A.*, **109**, 13188-93 (2012).
- [3] R. C. Moffet et al., *Analytical Chemistry*, **82**, 7906-7914 (2010).

MISCIBILITY OF DIFFERENT TYPES OF ORGANIC AEROSOL

F. Mahrt (PSI & UBC), Y. Huang, E. Newman (UBC), M. Ammann (PSI), A. K. Bertram (UBC)

Atmospheric aerosol particles often contain primary organic aerosol (POA) and secondary organic aerosol (SOA) components. Here, we investigate the miscibility of a large range of POA and SOA proxies that controls phase separation in organic aerosol.

A large mass fraction of tropospheric aerosols is composed of organic aerosol (OA), which is important for air pollution and climate. OA comprises primary organic aerosol (POA) and secondary organic aerosol (SOA) constituents [1]. POA denotes particles that are directly emitted into the atmosphere, whereas SOA is formed within the atmosphere, mostly through oxidation of volatile organic compounds, followed by gas-particle partitioning of the reaction products [1, 2]. The elemental oxygen-to-carbon (O:C) ratio is frequently used to categorize OA. For instance, measurements have detected hydrocarbon-like organic aerosol (HOA) with $0.02 \leq \text{O:C} \leq 0.26$ as a main component of POA, while the O:C ratio of SOA ranges from ~ 0.32 to 1.32 [3]. When HOA and SOA become internally mixed within individual aerosols, particles with one or two phases can form. In order to predict the role of OA for air pollution and climate, knowledge on the miscibility of these aerosols is crucial, as the miscibility impacts many processes including heterogeneous chemistry, gas-particle partitioning and in turn particle growth and size distribution, ultimately affecting climate. If HOA+SOA are completely miscible the presence of HOA seed particles enhances the SOA formation, by providing additional OA mass for semivolatile organic compounds to partition into. In contrast, such an enhancement is absent, if internal mixtures form two distinct aerosol phases. Here, we have investigated the miscibility of 13 HOA with 21 SOA species as a function of relative humidity (RH), using optical microscopy.

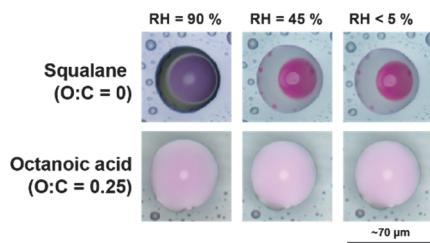


Fig. 1: Images of HOA+SOA particles at different RH (columns), where 2,5-hexanediol (O:C = 0.33) was used as SOA proxy and HOA proxies are indicated.

Fig. 1 shows exemplary microscopy images, for HOA+SOA mixtures, revealing that particles with either one or two phases can form, depending on the O:C ratio of the components and the RH.

Fig. 2 summarizes the number of liquid phases observed in our experiments at 5% RH, for all HOA+SOA mixtures tested, revealing distinct regions in the O:C phase space where either one or two phases form. Specifically, if the O:C ratio of the HOA was below 0.1, we almost always observed two liquid phases when mixing with SOA (O:C ≥ 0.3), as indicated by the hashed region. This observation is independent of RH for $0\% \leq \text{RH} \leq 90\%$ (not shown). Mixing two HOA species (O:C ≤ 0.29), always resulted in one liquid phase, independent of RH. For HOA with O:C ≥ 0.1 and SOA with O:C ≥ 0.3 , one or two liquid phases were observed, depending on the functionality of the constituents and the RH.

Overall, our results suggest that low-O:C HOA does not mix with SOA and hence does not enhance the SOA yields within the atmosphere. The presence of medium-O:C HOA, on the contrary, can enhance atmospheric SOA yields when mixing with SOA, depending on the functionalities of both the HOA and the SOA component and the ambient RH.

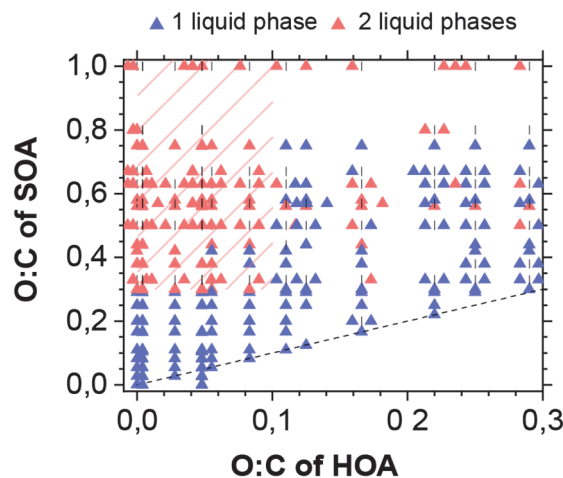


Fig. 2: Number of liquid phases observed for HOA+SOA mixtures as a function of their O:C ratio at $< 5\%$ RH.

E. N. acknowledges funding through UBC's WLIURA award (grant no. 10045). This work is part of a project that has received funding from the European Union's Horizon 2020 research and innovation program under the Marie Skłodowska-Curie grant agreement no. 890200 (F. M.).

- [1] J. L. Jimenez et al., *Science*, **326**, 1525 (2009).
- [2] M. Hallquist et al., *Atmos. Chem. Phys.*, **9**, 5155-5236 (2009).
- [3] M. R. Canagaratna et al., *Atmos. Chem. Phys.*, **15**, 253-272 (2015).

SPONTANEOUS REDOX REACTION ON SOLVATING INORGANIC AEROSOL

X. Kong (Univ. Gothenburg), I. Gladich (QEERI), D. Castarede, E. Thomson (Univ. Gothenburg), A. Boucly (PSI LEC & LUC), L. Artiglia (PSI LSK & LUC), M. Ammann (PSI), J. Pettersson (Univ. Gothenburg)

A surface-promoted sulfate-reducing ammonium oxidation reaction has been discovered to spontaneously take place on typical aerosol surfaces during water solvation and reveal that unique chemistry occurs on the surface.

Gas-particle interfaces play important roles in the atmosphere and directly influence many atmospheric processes. However, as interfacial processes take place on molecular scales, classical bulk thermodynamic theories are often insufficient to describe interfaces. For example, hygroscopic substrates are understood to solvate at a deliquescence relative humidity (DRH), but modern observational techniques have revealed that reversible water adsorption and reversible ion solvation already take place at a relative humidity (RH) lower than the DRH [1]. Explanations for such pre-deliquescence behavior can be rooted in strictly accounting for the unique physicochemical characteristics of surfaces [2]. These interfacial processes are challenging to characterize and are often overlooked in current atmospheric chemistry.

In this study, a novel surface-promoted redox reaction during salt solvation has been discovered by using ambient pressure X-ray photoelectron spectroscopy (APXPS). Classical and first-principle molecular dynamics were performed to support the characterization of the solvation process. Ammonium sulfate is used as the salt in this study, which is a common and important proxy for atmospheric inorganic aerosol.

Fig. 1 shows the photoelectron spectra for sulfur 2p and nitrogen 1s electrons at dry (RH = 3%), pre-deliquescence (RH = 48%) and full deliquescence (RH = 78%), including transient and steady state conditions.

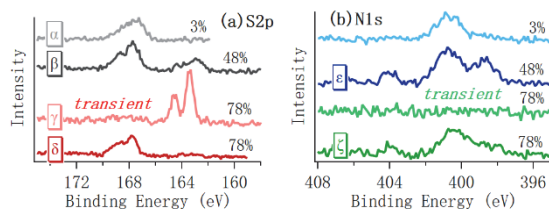


Fig. 1: (a) S 2p and (b) N 1s XPS peaks measured at RHs of 3, 48 and 78%. The photon energy was set to 435 eV for sulfur XPS and 665 eV for nitrogen XPS. The binding energies were aligned with C 1s at 284.8 eV.

Fig. 2 presents the peak assignments of the XPS spectra. At the lowest RH, the only features observed are the expected sulfate (SO_4^{2-}) doublet with the sulfur $2p_{3/2}$ peak around 167.5 eV (Fig. 2a, spectrum α) and the ammonium (NH_4^+) peak at ~ 401.0 eV. As the RH is increased to 48%, additional doublets of reduced sulfur species

(S^0), including elemental sulfur (S^0 with $2p_{3/2}$ around 163.2 eV) and bisulfide (HS^- with $2p_{3/2}$ around 162.5 eV) become visible (Fig. 2b, spectrum β). Two additional nitrogen-containing components also appear with increasing RH: nitrous acid (HONO) at ~ 404 eV and dissolved ammonia (NH_3) at ~ 399 eV (Fig. 2e, spectrum ϵ). At RH = 78%, where full deliquescence occurs a dramatic full conversion from SO_4^{2-} to S^0 is observed (Fig. 2c, spectrum γ) during the deliquescing transient period.

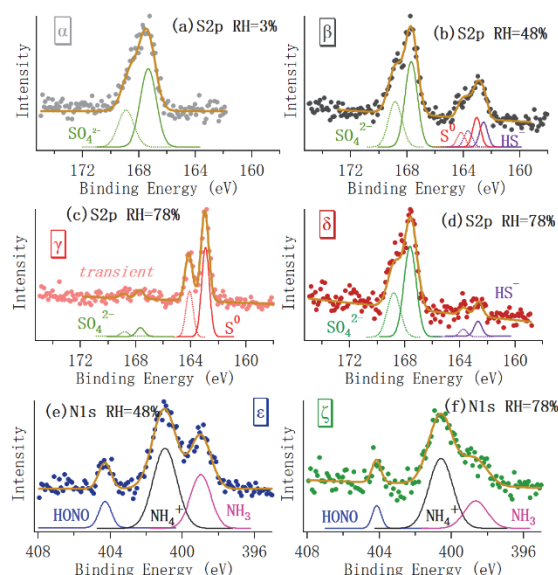


Fig. 2: Fitting results of the spectra shown in Fig. 1. At RH = 3%, a SO_4^{2-} doublet (a) is observed. At RH = 48%, S^0 and HS^- doublets (b) and HONO and NH_3 peaks (e) appeared. At RH = 78%, where full deliquescence occurred, most sulfate transferred to S^0 (c) and no nitrogen species could be found. When deliquescence was complete, the sulfur region was dominated by sulfate again (d) and nitrogen species reappeared (f).

As the deliquescence process proceeds and a new steady state is reached, the SO_4^{2-} reappears and only a small amount of HS^- remains on the surface. Importantly, a series of measurements were performed to evaluate the influence of X-ray beam damage, and the results confirmed that beam induced artifacts have not contributed to and/or influenced the observations.

We acknowledge funding from the Swedish Research Council (Grant 2015-04212).

- [1] X. Kong et al., J. Phys. Chem. C., **124**, 5263-5269 (2020).
- [2] D. Castarede et al., Atmos. Chem. Phys., **18**, 14939-14948 (2018).

IN SITU XPS AND XAS CHARACTERIZATION OF IRON IN AQUEOUS SOLUTIONS

L. Artiglia (PSI LSK & LUC), I. Gladich (QEERI), S. Chen, H. Yang (PSI & ETHZ), A. Boucly (PSI LEC & LUC), J. A. van Bokhoven (PSI LSK & ETHZ), M. Ammann (PSI)

This work shows in situ characterization of ferrous and ferric ions aqueous solutions, and of Fenton's reagents by means of liquid jet x-ray photoelectron and absorption spectroscopies.

The fundamental characterization of iron complexes in aqueous solutions is of paramount importance in the study of Fenton's chemistry. The reaction between Fe^{2+} ions and hydrogen peroxide, also known as Fenton's reaction, produces either highly-valent iron species (ferryls, FeO^{2+}) through a two-electron oxidation [1], or Fe^{3+} and $\cdot\text{OH}$ radicals, through a one-electron transfer [2]. The preferential formation of FeO^{2+} or Fe^{3+} reflects on the course of oxidative chemistry. Fe^{2+} and peroxides are present both in vivo and in the environment. Historically, it has been demonstrated that the one-electron mechanism plays a crucial role in aqueous environments [3]. However, recent experiments claim that, due to the partial hydration sphere of Fe^{2+} at the water-air interface, ferryls are preferentially formed when gaseous hydrogen peroxide is dosed [4]. The aim of this work is to use surface sensitive techniques (x-ray photoelectron spectroscopy –XPS- and near edge x-ray absorption fine structure spectroscopy –NEXAFS-) to investigate reference iron solutions and better understand Fenton's chemistry. Hybrid molecular dynamics calculations have been used to investigate stable iron complexes in solutions and complement the experimental data. Photoemission and absorption spectra were acquired on liquid filaments (diameter of approx. 25 μm) containing 300 mM Fe^{2+} and Fe^{3+} solutions, generated in vacuum by means of a commercial quartz nozzle injector. After acquisition of NEXAFS scans across the Fe $L_{2,3}$ edge, resonant energies for both oxidation states of iron could be detected and were used to scan the valence band (VB). Scanning the VB across an absorption threshold is known as resonant photoemission (ResPES), and provides insights into the contributions of different atomic species to the electronic states in the valence region. In this specific case, the main goal was to identify the molecular orbitals of iron ions and investigate their resonance.

Fig. 1a shows that Fe^{2+} and Fe^{3+} in aqueous solutions display similar behaviors as in solids (e.g. oxides). This means that the crystal field should be similar (O^{2-} and H_2O are weak ligands) [5,6]. Both ions are in an octahedral field and high spin complexes (small Δ_0) form. Hybrid MD calculations (Fig. 1a insets) display stable aquo-complexes within 0.5 ps. Both complexes are homogeneously distributed in the water slab. Interestingly, in the case of Fe^{3+} , some simulations show that one proton can be transferred to a neighbor water molecule forming $\text{Fe}(\text{OH})(\text{H}_2\text{O})_6^{2+}$. Fig. 1b-c show ResPES profiles, which were deconvoluted using the molecular

orbitals (MO) of water (from reference spectrum) and iron t_{2g} and e_g orbitals with the proper occupation and splitting. The resonant intensity from the iron orbital matches pretty well the absorption profile of iron reference spectra (Fig. 1a). Interestingly, Fe^{2+} displays a second (unknown) resonant peak. Further calculations are in progress to fully characterize these solutions and help explaining the results obtained with Fenton's reagents.

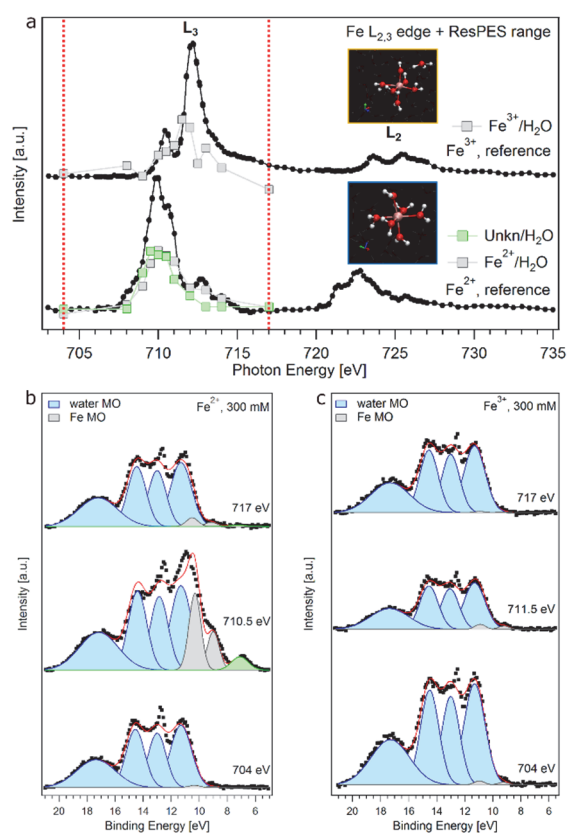


Fig. 1: (a) Fe $L_{2,3}$ NEXAFS of Fe^{2+} and Fe^{3+} 300 mM solutions. Resonant features in the VB are also reported. Insets show stable aquo-complexes calculated by MD ; (b, c) ResPES of the VB for Fe^{2+} and Fe^{3+} , respectively.

- [1] F. Haber, J. Weiss, Proc. Roy. Soc., A, **134**, 332 (1934).
- [2] W. C. Bray, M. H. Gorin, J. Amer. Chem. Soc., **54**, 2124 (1932).
- [3] J. J. Pignatello, et al., Crit. Rev. Environ. Sci. Technol., **36**, 1 (2006).
- [4] S. Enami, et al., PNAS, **111**, 623 (2011).
- [5] L. R. Merte, et al., J. Phys. Chem. C, **119**, 2572 (2015).
- [6] T. Droubay, S. A. Chambers, Phys. Rev. B, **64**, 205414 (2001).

A LINE DRAWN FOR PHOTOCHEMICAL REACTIONS IN AEROSOL PARTICLES

P. A. Alpert (PSI), K. Kilchhofer (PSI & ETHZ), M. Ammann (PSI)

Soluble transition metals can be complexed with carboxylate compounds in aerosol particles and become photochemically active. The balance between Fe and Cu in carboxylate complexes drastically impact the amount and production rate of radicals.

Aerosol particles from a variety of natural or anthropogenic sources contain trace amounts of soluble iron and copper. As an example, they amounted to 20 and 3 ng m⁻³ (air), respectively, in Padova, Italy with a total aerosol concentration on the order of 10 μg m⁻³ (air) [1]. The formation of radicals in atmospheric particles containing transition metals is primarily initiated by absorption of sunlight followed by photochemical reactions. Despite their trace amount, Fe photochemical cycling in the presence of Cu yields a significant amount of radical production and loss of organic matter due to photodissociation [2]. To better understand radical production from these metal-organic particles, we investigated single particles composed of iron(III)-citrate, copper(II)-citrate, and citric acid in an in-situ photochemical reactor coupled to X-ray spectromicroscopy instrumentation. First, light causes iron(III)-citrate to dissociate into an organic radical and a reduced iron ion with an oxidation state of +2. Organic radicals react with oxygen to form HO₂ and other reactive oxygen species (ROS) that reoxidize iron back to a +3 oxidation state, which can then re-complex with citric acid and reform iron(III)-citrate. This cycle is hypothesized here to be impacted by a dark reaction with copper, i.e.



This may cause a depletion of light absorbing compounds and a shutdown of reactive cycling and radical formation. As in our previous studies [3, 4], we observed the iron(III) fraction out of the total iron, β , to quantify photochemical reactive cycling in an X-ray microscope. It was found that at low relative humidity, $RH < 60\%$, oxygen could only penetrate within a few nanometers of the particle surface resulting in a high concentration of ROS and organic radicals, the latter of which also had a long life time.

Fig. 1 shows a map of β for multiple particles in a $7 \times 7 \mu\text{m}$ field of view after UV irradiation and allowing for dark reoxidation for ~ 1 hr. Particles larger than about $1 \mu\text{m}$ in diameter oxidized near their surface and remain reduced in their interior indicated by the red and green color, respectively. The black dashed lines are $0.5 \mu\text{m}$ in length and superimposed on 3 differently sized particles, of which the smallest is $< 1 \mu\text{m}$ in diameter. This is direct evidence of a sharp concentration gradient of oxidized iron delineated at about $0.5 \mu\text{m}$ and remaining for a long time.

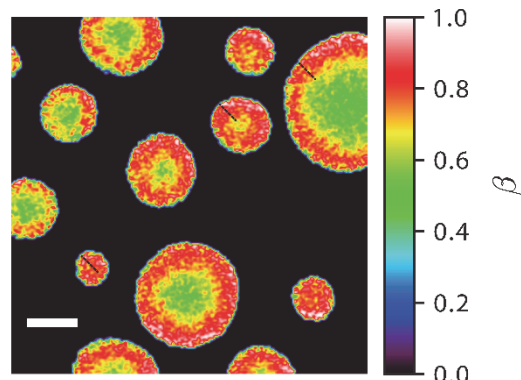


Fig. 1: Image of the iron(III) fraction, β , of particles following 10 min of UV irradiation and 1 hour of reoxidation at $RH = 50\%$. The white scale bar is $1 \mu\text{m}$. The black dashed lines are $0.5 \mu\text{m}$, which is likely the depth below the surface where radical cycling occurs.

These results imply that photochemical cycling in iron and copper containing organic particles is limited not only by chemical reaction but also the molecular diffusion of oxygen from the gas phase and through the particle. When particles without copper were subjected to the same photochemical cycling and RH , oxygen penetration was $0.01 \mu\text{m}$, much more shallow by comparison. This means that photochemical cycling in copper containing particles was much slower and allowed for more time for oxygen to diffuse further into the bulk of particles. This is in support of our hypothesis and reaction (1), that the presence of copper can slow photochemical reactive cycling. In future work, these data will be used to continually improve photochemical reaction and diffusion models [4, 5]. This will yield fundamental physical and chemical parameters to more accurately predict radical production in atmospheric particles.

We acknowledge funding from the Swiss National Science Foundation (Grant 188662).

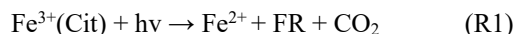
- [1] A. Tapparo et al., *Chemosphere*, **231**, 125025 (2020).
- [2] C. Weller et al., *Environ. Sci. Technol.*, **48**, 5652-5659 (2014).
- [3] P. A. Alpert et al., *Nat. Comm.*, *accepted manuscript* (2020).
- [4] J. Dou et al., *Atmos. Chem. Phys.*, **21**, 315-338 (2021).
- [5] T. Berkemeier et al., *Atmos. Chem. Phys.*, **17**, 8021-8029 (2017).

CONSTRAINING PHOTOCHEMISTRY IN ORGANIC AEROSOL WITH CO₂

K. Kilchhofer, L. Iezzi (PSI & ETHZ), T. Berkemeier (MPIC), S. Bachmann, P. A. Alpert, M. Ammann (PSI)

Photolysis of iron-carboxylate complexes in viscous organic aerosol produces reactive oxygen species (ROS). CO₂ monitoring in flow tube experiments and a kinetic multi-layer model may allow assessing the magnitude of ROS formation.

Reactive oxygen species (ROS) likely affect human health via inducing oxidative stress upon inhalation. Recent work in our group showed that photolysis of transition metal complexes in organic aerosol (OA) may form carbon-centered free radicals (FR), which react with oxygen to form peroxy radicals (i.e. ROS) [1-2]. This, in combination with low diffusivity in viscous OA particles, leads to anoxic conditions and only releases ROS when higher relative humidity (RH) is reached (upon inhalation in the lung). Taking the example of iron citrate (Fe-cit), absorption of radiation induces ligand-to-metal charge transfer, which results in emission of CO₂ to the gas phase:



In case of citrate, the FR react with oxygen leading to elimination of HO₂. HO₂ then oxidizes Fe²⁺ back to Fe³⁺. In extension to previous coated-wall flow tube experiments [3], we measured CO₂ in the gas phase as direct monitor of the Fe-cit photolysis rate. Figure 1 depicts CO₂ mixing ratios of experiments after reaching steady state at different RH. At RH = 30 %, the CO₂ mixing ratio is lowest and at higher RH we observed a similar steady-state CO₂ emission into the gas phase. This resulted from a combination of faster diffusion from the bulk to the surface of the film and from larger re-oxidation of Fe²⁺ to Fe³⁺ that increases the steady state Fe-citrate concentration.

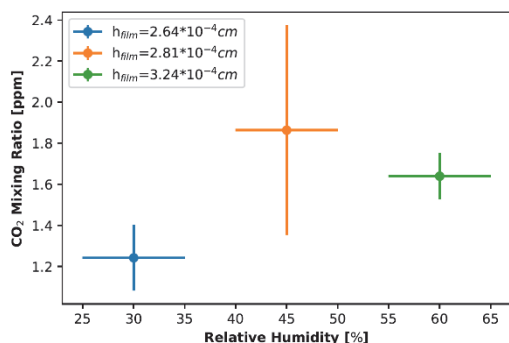


Fig. 1: Scatter plot of the mean CO₂ mixing ratios of a 5 min interval as a function of RH at steady state. The Fe-citrate film thickness h_{film} of each experiment in the flow tube slightly changes due to the varied RH. The vertical bars represent the standard deviation of each irradiation period and the horizontal bars the uncertainty in RH.

The measurements were used to inform the newly accommodated Kinetic Multiphase Meta Model (KM3) from KM-GAP [4]. It explicitly treats all steps of mass transport and chemical reaction of semi-volatile species partitioning between gas phase, particle surface and particle bulk. Here, we started to implement a simplified Fe-citrate photochemistry scheme including consideration of the flow tube configuration. The CO₂ production at three different RH, where the photolysis frequency (j) for R1 equals 0.0613 s⁻¹, while all other parameters (rate coefficients, diffusion coefficients) were reported previously [2], are modelled in KM3 and plotted in Fig. 2 along with the experimentally determined CO₂ release at RH = 45 %. It qualitatively agrees with the experimental data indicating a strong response of the model output to the RH, likely an effect of the changing viscosity [2]. Further analysis should also take into account the response time of the CO₂ analyzer.

The next steps will be step-by-step extensions to the chemical reaction scheme and the representation of the microphysical parameters such as bulk diffusion so that we will be able to properly model the photochemical degradation of Fe-citrate in an organic aerosol with KM3. This will be accompanied by mass spectrometry to follow the degradation of OA and the formation of products and STXM/NEXAFS experiments, targeted at understanding feedbacks between transition metal complex photochemistry, OA evolution and ROS formation.

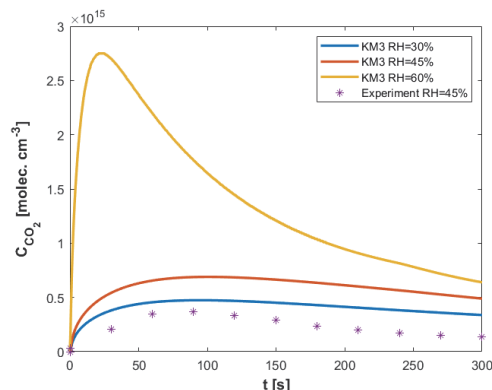


Fig. 2: CO₂ production in three different RH KM3 model scenarios with the result of one CWFT experiment at RH = 45 % ($t = 0$ defines the irradiation onset).

We acknowledge funding from the Swiss National Science Foundation (Grant 188662).

- [1] P. A. Alpert et al., Nature Comm., in press (2021).
- [2] J. Dou et al., ACP, **21**, 315 (2021).
- [3] P. Corral Arroyo et al., Environ. Sci. Technol, **52**, 7680 (2018).
- [4] M. Shiraiwa et al., ACP, **12**, 2777 (2012).

IRON(III)-CITRATE PHOTOLYSIS INDUCED CONVERSION OF NO₂

L. Iezzi, K. Kilchhofer (PSI & ETHZ), M. Ammann (PSI)

Past studies suggested photosensitized reduction of nitrogen dioxide (NO₂) on organic surfaces as a source of nitrous acid (HONO). Here, we assess the NO₂ conversion driven by iron (III)-citrate photochemistry in secondary organic aerosol proxies.

Nitrous acid (HONO) is a major source of the hydroxyl radical (OH), which plays a role in ozone and secondary aerosol formation in polluted air [1]. Earlier efforts focused on the role of triplet excited states of photosensitizers in oxidation of organic substrates and reduction of NO₂ to HONO [2]. However, despite many studies, to date the formation mechanism of HONO in the atmosphere is still not completely understood [2]. Organic compounds are major components in atmospheric aerosol particles and have received recent attention as potential ligands for iron(III) complexation [3]. The resulting complexes are important chromophores to initiate radical chemistry in the aerosol phase. The goal of this work is to observe the impact of peroxy radicals, which derive from iron(III)-citrate (Fe-cit) photochemistry, on the multiphase chemistry of NO and NO₂. Citric acid (CA) is an established proxy for oxygenated atmospheric organic matter [3]. The experiments were performed using a coated wall flow tube (CWFT), an alkaline trap for HONO, chemiluminescence (CLD) and infrared (NDIR) analyzers for NO_x and CO₂ detection, respectively. The CLD features two channels: one reduces the oxidized NO_y, i.e. NO₂ and HONO, to NO that undergoes the chemiluminescence reaction. This channel measures the sum of NO, NO₂ and HONO. The other one measures NO only.

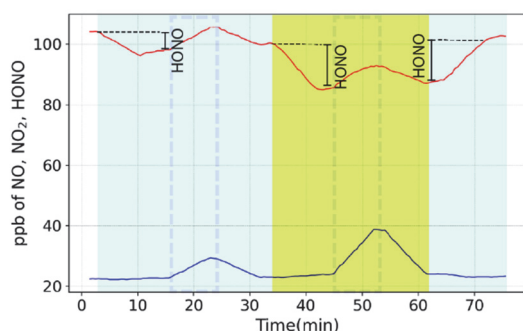


Fig. 1: Photoenhanced formation of HONO from exposure of a humic acid film to a mixture of NO (blue line) and NO₂ (red line) with the alkaline trap bypassed (dashed region), either in the dark (azure period) or under UVA irradiation (yellow period).

Fig. 1 shows the results of a reference experiment performed at 78% relative humidity (RH) with a 0.5 mg humic acid (HA) film. As obvious from Fig.1, upon switching on the lights and keeping the HONO trap inline, NO₂ dropped by about 15 ppb rather than 6 ppb in

the dark period. When bypassing the HONO trap, we observe an increase in both NO and NO₂ channels from partial reduction of HONO in the inlet of the instrument. While generally consistent with earlier work [2], HONO production could not be quantified due to the lack of a more selective HONO analyzer.

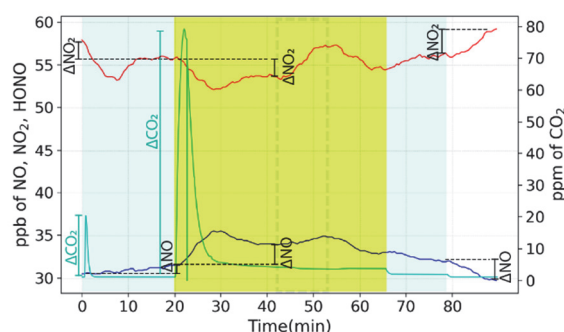


Fig. 2: Effect of UVA irradiation on the evolution of NO (blue), NO₂ (red) and CO₂ (azure) signals during an experiment with Fe-cit/CA. Shadings as in Fig. 1.

Fig. 2 shows the results of a similar experiment, but with 142 mg of a film composed of a 1:10 mixture of Fe-cit and CA, which forms an acidic aqueous solution (pH ≈ 1). In order to track the photochemical turnover, we monitored the CO₂ resulting from decarboxylation following photoexcitation of Fe-cit [3]. In contrast to the case of HA, the NO₂ drop in response to switching on light was accompanied by the formation of NO. Several hypotheses could explain this observation: photolysis of Fe-cit results in the formation of Fe²⁺ and HO₂ radicals. If HONO would form from the reaction of HO₂ with NO₂, it may further decompose to NO and NO₂ in acidic aqueous solution [4]. In turn, HO₂ could act as oxidant towards NO, while Fe²⁺ could act as reductant towards NO₂. Apart from the development of a more selective HONO detection technique, we will use explicit modelling of the aqueous phase chemistry to assess the interplay between nitrogen oxides and Fe-cit photochemistry.

We acknowledge funding from the Swiss National Science Foundation (Grant 188662).

- [1] N. K. Scharko et al., *Environ. Sci. Technol.*, **48**, 1991 (2014).
- [2] K. Stemmler et al., *Nature*, **440**, 195 (2006).
- [3] J. Dou et al., *Atmos. Chem. Phys.*, **21**, 315 (2021).
- [4] J. Baker et al., *Phys. Chem. Chem. Phys.*, **1**, 683 (1999).

PYRUVIC ACID KETO/GEM-DIOL EQUILIBRIUM: EXPERIMENT AND THEORY

A. Boucly (PSI LEC & LUC), L. Artiglia (PSI LSK & LUC), H. Yang (PSI & ETHZ), A. Roose (Univ. Lille, CNRS & PSI), A. S. P. Gomes, V. Vallet (Univ. Lille & CNRS), M. Masella (CEA Saclay), M. Ammann (PSI)

The surface properties of pyruvic acid aqueous solutions have been studied experimentally by liquid jet X ray Photoelectron Spectroscopy (XPS) and theoretically through molecular dynamics simulations and relativistic quantum methods.

Pyruvic acid is the simplest α -keto acid. It plays an important role in the metabolism of carbohydrates and has an important role in metabolic pathways, such as gluconeogenesis, transamination and fermentation. It can also be involved in enzyme-catalyzed intracellular phenomena and converted into fatty acids or energy [1]. Pyruvic acid is also found in tropospheric air, especially in the boundary layer of vegetated regions and thus plays a role in atmospheric chemistry as a product of oxidation of volatile organic compounds [2-3]. Its condensed phase photochemistry is an important source of radicals in aerosol particles [3].

Yet being an α -keto acid, pyruvic acid exists in several different forms depending on several equilibria such as the keto/enol and the keto/gemdiol equilibria, which is the focus of the present work. Several parameters affect the keto/gem-diols equilibrium such as the pH, the pyruvic acid concentration and the temperature. The higher they are, the more the keto form is favored. While relatively well established for the bulk aqueous phase, the relative abundance of these species has never been assessed at the aqueous solution – air interface.

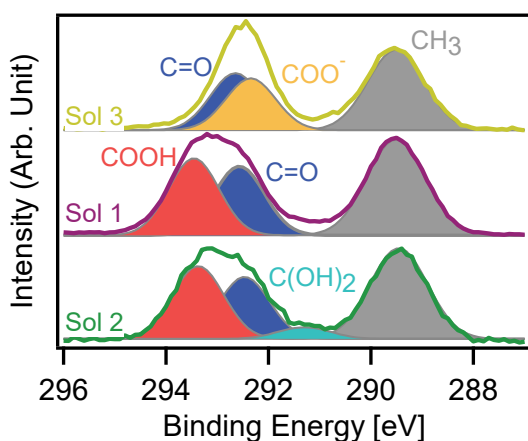


Fig. 1: C 1s XPS spectra of pyruvic acid solutions: Solution 1: pH 1.5, 0.1 M (Sol 1) in purple; solution 2: pH 1.5, 0.01 M (Sol 2) in green; solution 3: pH 3.5, 0.1 M (Sol 3) in gold. The grey component corresponds to the methyl group (CH_3), the light blue to the gem-diol ($\text{C}(\text{OH})_2$), the dark blue to the keto ($\text{C}=\text{O}$), the amber to the carboxylate (COO^-) and the red to the carboxylic (COOH) group.

We therefore performed liquid jet XPS experiments at the SIM beamline at SLS to obtain C 1s spectra as a function of the photoelectron kinetic energy, thus as a function of probe depth into the solution. Systematically varying the solution concentration and pH allows identifying the dominant form within the pyruvic acid keto/gem-diol equilibrium at the aqueous solution – vapor interface. The measured binding energies can then be compared to those estimated by theory. Fig. 1 shows C 1s spectra taken for three solutions excited by 448 eV photon energy, thus with 160 eV photoelectron kinetic energy and thus 1 nm probe depth. For all solutions, there is no change of the methyl group shown in black. The first solution at low pH (pH=1.5) and higher concentration ($C=0.1$ M) exhibits only the keto form shown in dark blue. Even if we are at low pH, the high concentration shifts the equilibrium towards the keto form, which may be different at the surface versus the bulk solution. However, by decreasing the concentration to 0.01M while keeping the same pH of 1.5 (solution 2), we observe a peak shown in light blue appearing below our keto group: the gem-diol form. When we increase the pH to 3.5 (solution 3), we observe the transition from a carboxylic acid (red peak) visible in the first two solutions to a carboxylate (amber peak). Thus with those measurements we have been able to determine the binding energy differences between all components of the keto/gem-diols equilibrium as a basis for comparison to the theory.

On the theoretical side, to rationalize the behavior of the different pyruvic species at the liquid water/vapor interface, molecular dynamics (MD) simulations are currently being performed in conjunction with sophisticated polarizable potentials. These simulations are then post analyzed using relativistic quantum chemistry methods allowing to estimate the C(1s) electron binding energies. These data can be directly compared to (or used to ease the interpretation of) electron binding energy measurements of the XPS experiments.

Funding via the Interlaboratory Postdoc program of the ENE division, PSI, is appreciated.

- [1] A. Lopalco et al., *J. Pharm. Sci.*, **105**, 664-672 (2016).
- [2] P. G. Eger et al., *Atmos. Chem. Phys.*, **20**, 3697-3711 (2020).
- [3] A. E. Reed Harris et al., *J. Phys. Chem. A.*, **121**, 3327-3339 (2017).

SURFACE PROPERTIES OF AQUEOUS RESORCINOL SOLUTIONS

H. Yang (PSI & ETHZ), L. Artiglia (PSI LSK & LUC), A. Boucly (PSI LEC & LUC), M. Ammann (PSI)

Surface active organic molecules may influence the organization of water molecules at the aqueous solution – air interface and influence the freezing behavior. We characterize the liquid vapor interface of resorcinol aqueous solutions by X-ray photoelectron spectroscopy (XPS).

Resorcinol (1,3-benzenediol) is a simple proxy for a range of phenolic compounds in the atmosphere resulting from oxidation of aromatic compounds or from pyrolysis of biomass. XPS allows differentiating the specific contributions by carbon at the OH substitution (C-OH) from that by the aromatic carbons in between (C=C). When using varying photon energies to excite the C 1s levels, photoelectrons are detected with varying kinetic energies and thus with different probing depth. As shown in Fig. 1a, for the case of a 2 M resorcinol solution, the contribution of the C-OH carbons to the total C 1s intensity is lower than expected based on the molecular structure (2:4) when measured at low kinetic energies. At higher kinetic energy, the proportions of the two different carbons are as expected. This implies an upward orientation of the resorcinol molecules on the surface due to preferential hydration of the OH groups, as depicted in Fig. 1b.

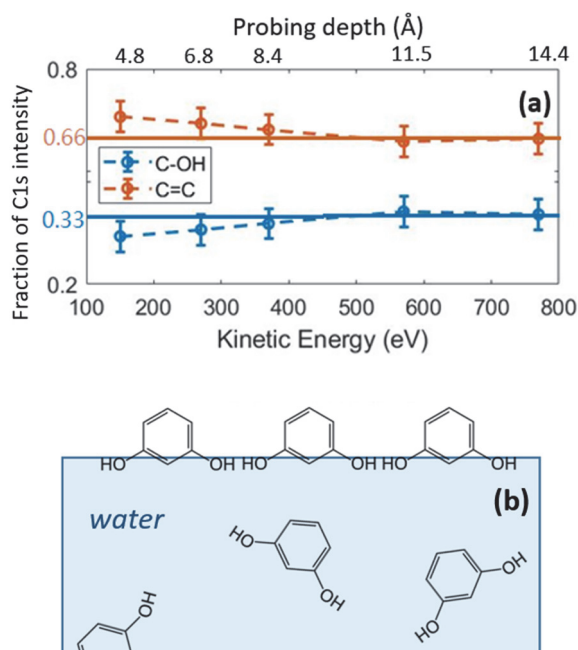


Fig. 1 a): The fractional contribution to the C 1s photoemission intensity of C-OH carbon (blue) and of C=C carbon (red), in comparison to the stoichiometric contributions (1/3 and 2/3, respectively, solid lines), as a function of photoelectron kinetic energy. **b):** Schematic illustration of resorcinol molecules at the aqueous solution – air interface.

Photoelectrons from the top-most C=C carbons reach the electron analyzer with less attenuation than those from the C-OH carbons, explaining the observed features in surface specific detection mode. According to a quantitative analysis of C 1s and O 1s spectra (not shown), the abundance of solute molecules on the interfacial region was about 10^{15} molecules cm^{-2} .

Valence levels of molecular orbitals are strongly affected by the physical environment of the molecules. They can be used to determine the effect of a solute on the local structure of water [1]. We measured valence spectra of the resorcinol solutions using 600 eV excitation photon energy, along with reference spectra of pure water and pure ice, shown in Fig. 2. Pure liquid water has a pronounced $3a_1$ peak and a smaller $1b_2$ feature. In contrast, for ice, the $3a_1$ peak is less pronounced. The Gaussian peak deconvolution based on Winter et al. [1] is shown in Fig. 2 for 2 M resorcinol and marked by shadings, with two peaks representing $3a_1$. A detailed analysis indicates that the coordination of water molecules in the aqueous resorcinol solution is more close to that of ice. Thus, the presence of these surface active molecules induces a tetrahedrally coordinated hydrogen bonding structure, which may facilitate the formation of ice in the atmosphere.

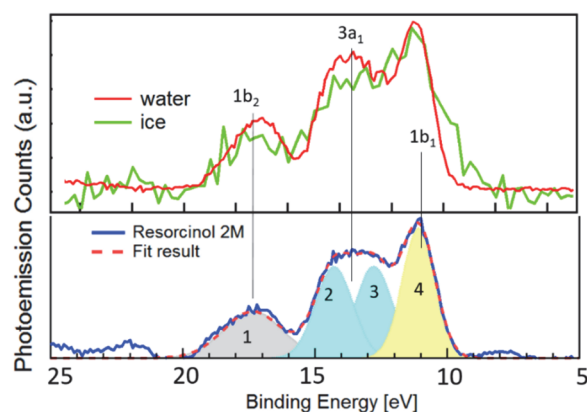


Fig. 2: Gaussian peak deconvolution of the valence spectrum of a 2 M aqueous resorcinol solution (blue, bottom panel). Liquid water (red) and ice (green) are shown for comparison (top panel), aligned with the $1b_1$ peak. All spectra are Shirley background subtracted.

We acknowledge funding from the Swiss National Science Foundation (Grant 169176).

[1] B. Winter et al., J. Phys. Chem. A, **108**, 2625 (2004).

TOWARDS FAST AND ULTRAFAST IODINE CHEMISTRY IN THE LIQUID PHASE

Y. Uemura, M. Ammann (PSI), T. Lind, D. J. Suckow (PSI NES), M. Nachtegaal, C. Milne, P. Johnson (PSI PSD)

In this project, we address the photochemistry of organo-iodine compounds in aqueous solution. Optical pump-probe experiments of the photolysis of CH_3I indicated the formation of an intermediate species at ~ 2 ns and of I_2 at ~ 50 ns.

Iodine compounds play important roles in environmental chemistry [1]. Organo-iodides coming from biologically active oceans undergo photolysis in the aqueous phase, leading to reactive iodine species in the gas phase, where they participate in ozone depleting catalytic cycles or are oxidized to climate relevant iodine oxide nanoparticles. Iodine is also an important element during severe accidents in nuclear power plants (NPPs) due to its volatility and high radiotoxicity. Organo-iodides may form from reactions of reactive iodine species with organic materials, e.g., paints, used in containments. CH_3I (methyl iodide, MI) is the most simple proxy for organo-iodides. In contrast to the gas phase [2], the photodissociation of MI in the liquid phase has been rarely studied [3]. In the contexts above, the population and the fate of dissociation fragments in solutions against reaction time need to be understood.

After MI absorbs UV light (< 280 nm), it decomposes to form a methyl radical and an iodine radical (I^0). I^0 is the starting point for various kinds of iodine products in water. First, we conducted photolysis experiments with 100 mM and 10 mM MI solutions under continuous UV irradiation, with I_2 and I_3^- quantified by UV-Vis absorption. As shown in Fig. 1, I_2 was the main product, but at 100 mM, a larger proportion of I_3^- was observed than at 10 mM. It seems that a secondary reaction such as $\text{I}_2 + \text{I}^- \rightarrow \text{I}_3^-$ occurred. Since the photolysis of MI yields just CH_3^* and I^0 , the potential source of I^- remains to be discussed in view of the many reported elementary reactions of iodine compounds [4].

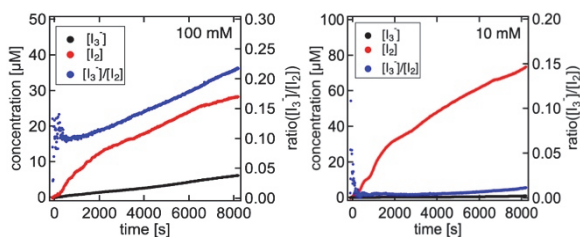


Fig. 1: The photolysis of methyl iodide (MI) in water at 100 mM MI (left) and 10 mM MI (right) at 260 nm, with an average UV power of ~ 1 mW. The concentrations of I_2 and I_3^- were estimated by the absorption at 450 nm and 350 nm, respectively.

Second, optical pump probe spectroscopy experiments were conducted at the Alvra beamline, SwissFEL. A femtosecond Ti:Sapphire laser was employed as a pump laser and its fundamental was tripled to excite MI. A

nanosecond laser with an optical parametric amplifier was employed as a probe laser. The probe wavelength was variable from 400 – 800 nm and its pulse duration was ~ 2 ns. The results indicate two distinct processes: The first was characterized by a fast rise and fall observed at 600 nm. This process should be related to the intermediate species formed just after photodissociation. The second process exhibited a slow increase of the absorption at 450 nm, which most likely originates from the formation of I_2 . A fast rise was also observed at 450 nm, which implies that the intermediate species should have a broad absorption peak.

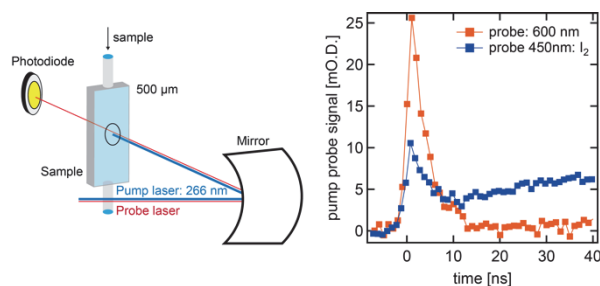


Fig. 2: The transient absorption experiment of the photolysis of MI in water: (left) a simplified illustration of the pump-probe setup at the Alvra beamline, SwissFEL; (right) the transient absorptions of the MI solution at 450 nm and 600 nm after the UV-excitation.

Based on these results, a reaction mechanism will be set up. The present continuous and transient optical absorption experiments will be extended towards transient x-ray absorption spectroscopy (XAS) directly targeted towards detection of the I^0 species not accessible by optical methods.

This project is financed by a PSI CROSS project co-funded by the ENE, NES and PSD divisions. MA acknowledges funding from the Swiss National Science Foundation (Grant 188662).

- [1] L. J. Carpenter et al., *Chem. Rev.*, **115**, 4015 (2015).
- [2] A. R. Attar et al., *J. Phys. Chem. Lett.*, **6**, 5072 (2015).
- [3] Y. Wang et al., *Chem. Phys. Lett.*, **633**, 126 (2015).
- [4] R. C. Cripps et al., *Nucl. Eng. Des.*, **241**, 4306 (2011)

INVESTIGATION OF AQUEOUS IODINE CHEMISTRY IN THE TROPOSPHERE

A. Roose (Univ. Lille, CNRS & PSI), M. Ammann (PSI), M. Reza, H. Finkenzeller, R. Volkamer (Univ. Colorado), C. Toubin, V. Vallet (Univ. Lille & CNRS), A. Tilgner, E. Hoffmann, H. Herrmann (TROPOS)

The presence of iodide in the troposphere and the stratosphere highlight the existence of iodine recycling mechanisms. We use the explicit aqueous-phase chemistry model CAPRAM to trace oxidation of iodide and reduction of iodate in the troposphere.

Field measurements have shown that iodine species (especially iodide (I^-) and iodate (IO_3^-)) in the stratosphere are more significant than firstly thought [1]. First, this may represent a direct or indirect sink for ozone in the stratosphere. Second, this indicates the presence of iodine cycling in the gas phase of the troposphere that prevents iodine from wet deposition. Third, given the short life-time of iodide against oxidation, this indicates the presence of recycling that reduces iodate, the most oxidized form of iodine, back to iodide, in both the troposphere and the stratosphere. The latter could include photochemistry or the so-called Bray Liebhafsky mechanism [2] in presence of H_2O_2 .

In order to obtain an overview over cycling of iodine in the troposphere, we have used the SPectral Aerosol Cloud Chemistry Interaction Model (SPACCIM) that is coupled to MCMv3.2 for the gas phase chemistry and to CAPRAM4.0 for explicit aqueous phase chemistry, which also includes a very detailed halogen chemistry module [3,4]. We have used a pristine ocean scenario to start with a relatively well defined system. We have further compared the cases of cloud-free, but aerosol containing air at low altitude with that of an all-day cloud forming upon updraft of the air to higher altitude.

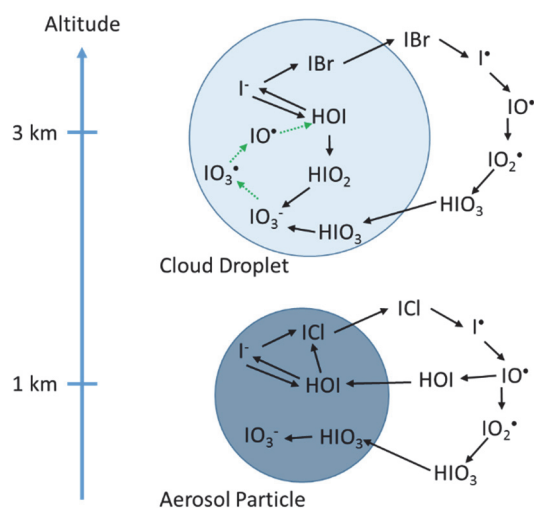


Fig. 1: Iodine cycling in the troposphere in a pristine oceanic air mass, in cloud free air at low altitude (bottom) and in a cloud (top) higher up. Only pathways with substantial rates are shown in black, the dashed green arrows indicate orders of magnitude lower rates.

Fig. 1 provides a summary of important pathways. As expected, initially I^- is rapidly oxidized by O_3 to HOI, but also there is fast reduction back to I^- by HSO_3^- (thus dissolved SO_2). However, at steady state, the main pathway for the further oxidation is via the gas phase by the formation of ICl from the reaction either of HOCl with I^- or of HOI with Cl^- . Once in the gas phase, ICl is photolyzed, and the resulting I atom is oxidized by ozone to IO. The reaction of IO with HO_2 is the source of HOI back to the aerosol phase. From IO, two subsequent reactions involving BrO and OH lead to HIO_3 , which dissolves and dissociates in the aqueous phase to form iodate. Based on the reactions included in CAPRAM, no reaction sequence reduces iodate to iodide at significant rates. After the air parcel has been uplifted to become a cloud, the gas phase cycling is still important through the formation of IBr by the reaction of I^- with HOBr, but also the oxidation in the aqueous phase by HOCl, O_3 and H_2O_2 becomes more significant (Fig. 1). Under these conditions, there is also a pathway of iodate reduction through the formation of IO_3 and IO radicals, which, however, features very low rates. In all simulations, the iodate to iodide ratio remains orders of magnitude higher than observed in field measurements [5].

We currently investigate the hypothesis that reaction of iodate with H_2O_2 that is part of the Bray Liebhafsky mechanism as described by Masimović et al. [2] could represent an important recycling pathway for iodate in the condensed phase. These reactions have not yet been characterized well enough for atmospheric conditions. Therefore, experiments will be performed, and these reactions will be included in CAPRAM to assess their impact on iodine speciation in aerosol and cloud water.

We acknowledge support by the French government through the Program "Investissement d'avenir" through the Labex CaPPA (contract ANR-11-LABX-0005-01) and I-SITE ULNE project OVERSEE (contract ANR-16-IDEX-0004) and CPER CLIMIBIO. MA acknowledges funding from the Swiss National Science Foundation (Grant 188662). RV acknowledges funding from the US National Science Foundation (Grants AGS-1951514, AGS-2027252).

- [1] T. K. Koenig et al., PNAS, **117**, 1860 (2020).
- [2] J. Maksimović et al., *Reac. Kinet. Mech. Cat.*, **130**, 655 (2020).
- [3] E. Hoffmann et al., *ACS Earth Space Chem.*, **3**, 771 (2019).
- [4] P. Bräuer et al., *Atmos. Chem. Phys.*, **19**, 9209 (2019).
- [5] A. Saiz-Lopez et al., *Chem. Rev.*, **112**, 1773 (2012).

IS IODIDE A SINK FOR OZONE IN THE STRATOSPHERE?

S. Gysin, L. Iezzi (PSI & ETHZ), A. Roose (Univ. Lille, CNRS & PSI), M. Reza, H. Finkenzeller, R. Volkamer (Univ. Colorado), T. Peter (ETHZ), M. Ammann (PSI)

Recent aircraft measurements report significant amounts of inorganic iodine in the lower stratosphere possibly representing a sink for ozone. Here, we examine the temperature dependent kinetics of the aqueous phase reaction of iodide with ozone.

Tropospheric multiphase redox reactions prevent poorly soluble gaseous iodine species from removal by wet deposition leading to injections of inorganic iodine into the lower stratosphere. Only recently, Koenig et al. [1] confirmed this by measuring gas phase iodine species as well as oxidized (iodate) and even reduced (iodide) particulate iodine in the lower stratosphere. This may influence stratospheric ozone depletion as iodide can directly destroy ozone (O_3) through an aqueous phase reaction [2] with O_3 , the temperature dependence of which is only poorly constrained.

The kinetic experiments in a trough reactor described by Artiglia et al. [4] allow measuring the loss of O_3 to aqueous iodide solutions indicated with the purple arrow in Fig. 1. The measured O_3 loss enables then to derive the uptake coefficient, γ_{O_3} , which describes the probability that an O_3 molecule is lost by reaction in the aqueous phase upon gas kinetic collision.

Assuming that the aqueous phase reaction is rate limiting, we used a quasi steady state resistance model [3] to relate measured γ_{O_3} to physical parameters of the reaction:

$$\gamma_{O_3} = \frac{4 \times H \times R \times T}{\omega_{O_3}} \times \sqrt{D_{l,O_3} \times [I^-]_{SS} \times k_l} \quad (\text{Eq. 1})$$

ω_{O_3} denotes the mean thermal velocity of the O_3 molecules in the gas phase, D_{l,O_3} the diffusion coefficient of ozone in the liquid phase, $[I^-]_{SS}$ the quasi steady state concentration of iodide in the aqueous phase, k_l the second-order rate coefficient of the ozone plus iodide reaction, H the Henry's law constant of O_3 in water, R the gas constant and T the temperature.

Fig. 1 shows the raw ozone data for one kinetic experiment performed with the trough reactor. We switched the ozone gas flow three times for 7 min from the bypass (green area) to the trough reactor (orange area), which enables to calculate a preliminary average γ_{O_3} . We performed such experiments for different temperatures (2, 10 and 18 °C), ozone mixing ratios (0.15 – 1 ppm) and iodide concentrations (1×10^{-4} – 1×10^{-3} M).

Fig. 2 agrees with the expectation from Eq. 1, as we observe a linear increase of the preliminary γ_{O_3} with the square root of the iodide concentration at all three temperatures, supporting the assumption of the aqueous phase reaction as rate limiting step. Further analysis will consider potential limitations by diffusion in the gas and aqueous phases and their correction. Using additional

measurements, an assessment of the temperature dependence of all parameters constituting γ_{O_3} as well as a chemical reaction model will allow determining the temperature dependence of the rate coefficient, k_l .

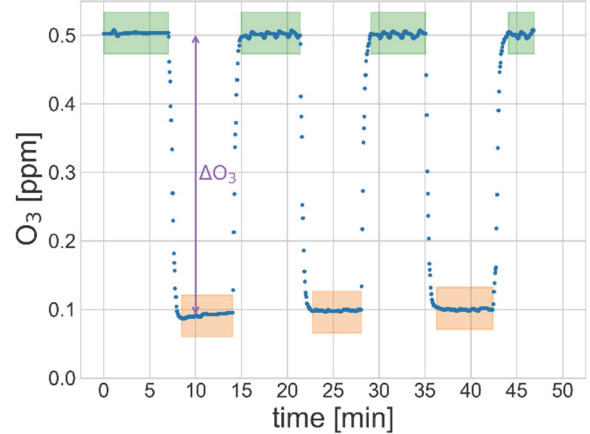


Fig. 1: Measured ozone mixing ratios during a kinetic experiment performed under quasi steady state conditions at 2 °C using a 1×10^{-3} M aqueous NaI solution.

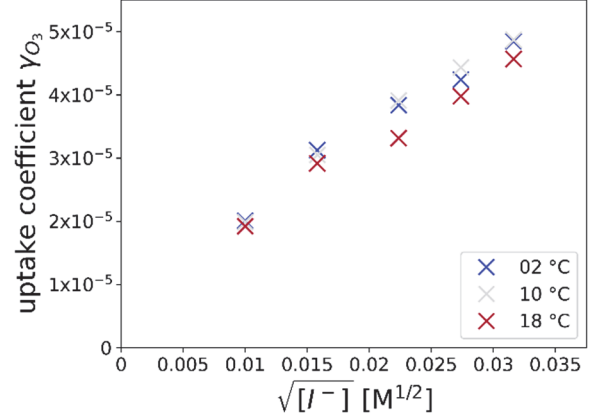


Fig. 2: Preliminary uptake coefficient γ_{O_3} versus the square root of the iodide concentration at 0.5 ppm O_3 and at different T .

Funding is acknowledged from the US National Science Foundation (Grants AGS-1951514, AGS-2027252) for RV and from the Swiss National Science Foundation (Grant 188662) for MA and LI.

- [1] T. K. Koenig et al., PNAS, **117**, 1860-1866 (2020).
- [2] L. J. Carpenter et al., Nat. Geosci., **6**, 108-111 (2013).
- [3] M. Ammann et al., Atmos. Chem. Phys., **13**, 8045-8228 (2013).
- [4] L. Artiglia et al., Nature Comm., **8**, 700 (2017).

PHOTOEMISSION OF AQUEOUS IODINE SPECIES: THEORY AND EXPERIMENT

A. Roose (Univ. Lille, CNRS & PSI), A. Boucly (PSI LEC & LUC), H. Yang, L. Iezzi (PSI & ETHZ), C. Toubin, V. Vallet, L. Halbert, A. S. P. Gomes, R. Opoku (Univ. Lille & CNRS), M. Ammann (PSI), L. Artiglia (PSI LSK & LUC)

The topic of interfacial enhancement of iodine species in aqueous aerosol particles is relevant for the ozone budget of the atmosphere. Surface sensitive photoemission experiments for aqueous iodide and iodate solutions are compared to theory.

Iodine species contribute substantially to the sinks of ozone in the troposphere and presumably as well in the stratosphere [1]. Earlier claims of iodide being enhanced at the interface [2] to sustain efficient ozone depletion chemistry has recently been challenged [3], similar to the case of bromide [4]. The behavior or impact of more oxidized iodine species has not been assessed yet so far at all. X-ray photoelectron spectroscopy (XPS) is ideally suited to explore electronic structure and surface propensity of such species at the interface of aqueous solutions.

The liquid jet XPS experiments have been carried out at the SIM beamline at the Swiss light source. The spectra shown in Fig. 1 were obtained with 0.2 M sodium iodide and sodium iodate. The iodate I 3d binding energy shows a shift of 5.1 eV from that of iodide. Analysis of spectra obtained at different photon energies to obtain their depth profile is currently ongoing.

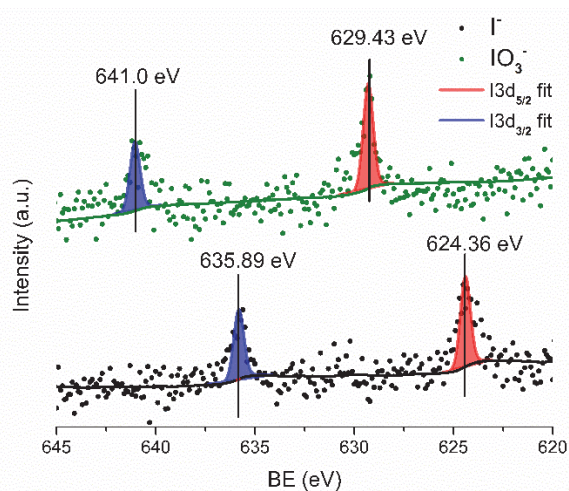


Fig. 1: I 3d XPS spectra of aqueous sodium iodide (0.2 M, bottom) and sodium iodate solutions (0.2 M, top) at $h\nu = 900\text{eV}$.

Following up from previous work with the valence levels of several halide species [5], theoretical computations are in progress to determine the spectra using the so-called Frozen Embedding Method where DFT SAOP is coupled with CVS-EOM-IP-CCSD/d-aug-dy-all.ac2vz via a molecular mean-field X2C including the Gaunt interaction [6]. The computation of the iodide core binding energies in the aqueous phase (represented by a 50 water molecules droplet model) has been carried

out for 50 classical molecular dynamics (MD) snapshots [5], from which mean values (μ) for the core binding energies have been determined (Fig. 2).

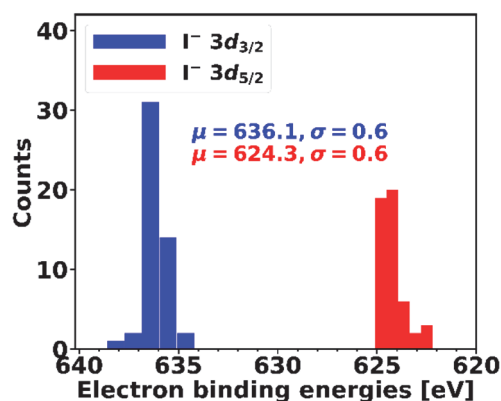


Fig. 2: Calculated 3d electron binding energy spectrum of $[\text{I}^- + (\text{H}_2\text{O})_{50}]$ (μ : mean value; σ : standard deviation).

Our mean theoretical binding energies, and the associated spin-orbit splitting of the I 3d band, are in very good agreement with the experimental spectra, demonstrating the suitability of the theoretical models for describing halides in solution. In the future, these calculations will be extended towards iodate and other intermediate iodine oxidation state species. Furthermore, the surface propensity of all species will be assessed with classical molecular dynamics simulations.

We acknowledge support by the French government through the Program “Investissement d’avenir” through the Labex CaPPA (contract ANR-11-LABX-0005-01) and I-SITE ULNE project OVERSEE (contract ANR-16-IDEX-0004), CPER CLIMIBIO (European Regional Development Fund, Hauts de France council, French Ministry of Higher Education and Research) and French national supercomputing facilities (grants DARI x2016081859 and A0050801859). We acknowledge funding from the Swiss National Science Foundation (Grant 188662).

- [1] T. K. Koenig et al., PNAS, **117**, 4 (2020).
- [2] S. Ghosal et al., Science, **307**, 563-566 (2005).
- [3] G. Olivieri et al., **122**, 910-918 (2018).
- [4] I. Gladich et al., J. Phys. Chem. Letters, **11**, 3422-3429 (2020).
- [5] Y. Bouchafra et al., PRL, **21**, 26 (2018).
- [6] L. Halbert et al., arXiv:2011.08549 (2020).

ALPINE ICE CORES – REPRESENTATIVE ARCHIVES OF PAST AIR POLLUTION

A. Eichler, T. M. Jenk (PSI), M. Legrand, S. Preunkert (UGA), M. Schwikowski (PSI & Univ. Bern)

An excellent agreement in the trend of air pollutants at different high-Alpine ice core sites during the period 1750-2015 was observed, showing that these ice cores are representative environmental archives of air pollution in Western and Southwestern Europe.

Different high-Alpine ice cores have been proven to contain well preserved records of past air pollution in Western Europe (e.g. [1,2]). However, a systematic comparison between different ice cores to investigate the spatial representativeness of single sites is lacking. Here we present the first study comparing long-term pollution records of all available high-Alpine sites for the period 1750-2015.

An excellent agreement in the ice-core concentration trends of all investigated pollutants (major ions, carbonaceous species, trace species) was observed between four high-Alpine sites (Col du Dome CDD, Colle Gnifetti CG, Fiescherhorn FH, and Grenzgletscher GG) (Fig 1). Records of exSO_4^{2-} (non-dust and non-sea salt SO_4^{2-}), F, Pb, and Cd mainly reflecting emissions from fossil fuel combustion, the aluminum industry, the use of leaded gasoline, and zinc smelters, respectively, peak during the 1970s and show a significant decrease afterwards. The strong decline reflects the efficacy of recent emission abatement efforts in the source regions of air pollution, mainly the western and southwestern European countries France, Switzerland, Italy, Germany, and Spain (e.g. [3]). Elemental and black carbon (EC, BC) records peak in the first half of the 20th century due

to vast emissions from coal burning.

In contrast to the six species discussed above, the increase in concentrations of NO_3^- , NH_4^+ and dissolved organic carbon (DOC) from traffic, agriculture, and the formation of secondary organic aerosols, respectively, occurred later, during the second half of the 20th century. Concentrations of these three species at the beginning of the 21st century are unprecedented in the context of the past 250 years. This is in strong contrast to the emission data of the precursor species NO_x and NH_3 from the source regions (e.g. [4]), peaking some when in the 20th century, slightly different for the two species. On the other hand, the observed recent decline in exSO_4^{2-} , F, Pb, Cd, EC, and BC concentrations is in reasonable agreement with model data based on such emission estimates (e.g. [3,5]).

This highlights the great value of such ice core records, providing a representative signal of air pollution being useful to complement or even constrain emission data of air pollutants.

- [1] S. Preunkert and M. Legrand, *Clim. Past.*, **9**, 1403 (2013).
- [2] M. Schwikowski et al., *J. Geophys. Res.*, **109**, 13709 (1999).
- [3] M. Legrand et al., *Geophys. Res. Lett.*, **47**, e2020GL087537 (2020).
- [4] R. Hoesly et al., *Geo. Mod. Dev.*, **11**, 369 (2018).
- [5] M. Engardt et al., *Tellus B*, **69**, 1 (2017).

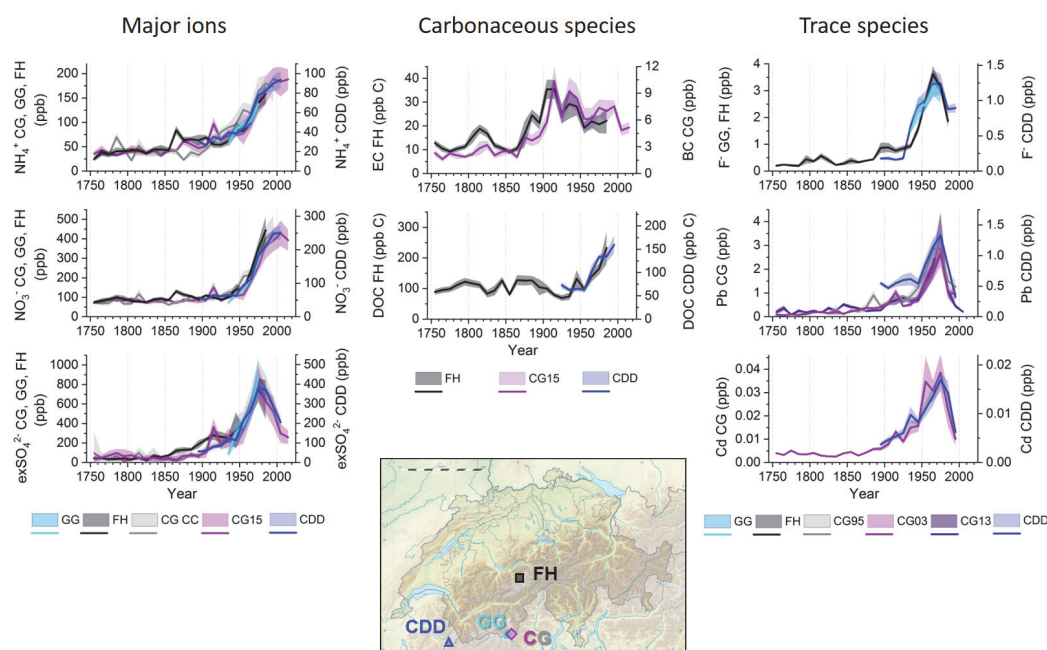


Fig. 1: Compilation of ice core concentration records from four sites (see text) for major ions NH_4^+ , NO_3^- , exSO_4^{2-} , carbonaceous species EC, BC, DOC, and trace species F, Pb, Cd covering the time period 1750-2015.

MODELING exSO_4^{2-} CONCENTRATIONS IN PRECIPITATION AT 4 ALPINE SITES

C. Andersson (SMHI), M. Engardt (SLB), T. M. Jenk (PSI), M. Legrand (UGA), T. Olenius (SMHI), S. Preunkert (UGA), M. Schwikowski (PSI & Univ. Bern), A. Eichler (PSI)

Atmospheric chemical transport modeling of exSO_4^{2-} in precipitation at different high-Alpine sites shows that depending on the spatial model resolution (50 km or 12 km), concentrations either differ (50 km) or compare well (12 km).

A good correspondence of exSO_4^{2-} (non-dust and non-sea salt SO_4^{2-}) concentration trends was observed at four Alpine ice core sites (Col du Dome CDD, Colle Gnifetti CG, Fiescherhorn FH, Grenzgletscher GG) [1] (Fig 1). This suggests that they are representative of a common emission source region (western and southwestern Europe) due to mixing of air masses before vertical transport to high elevation. However, the observed factor of ~ 2 between CDD and the other sites is unresolved so far. The most likely explanation is a higher proportion of winter snow at the CDD site [2]. Here we use an atmospheric chemical transport model to simulate exSO_4^{2-} concentration in precipitation at the different sites and test, whether such a concentration factor is also observed in models.

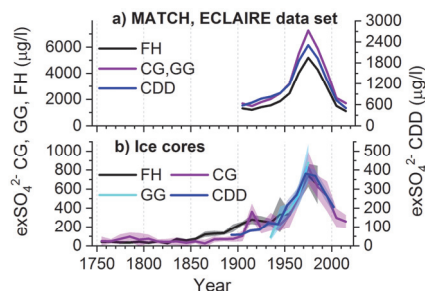


Fig. 1: Comparison between a) modeled and b) measured exSO_4^{2-} concentration records at 4 ice core sites.

The trend in the exSO_4^{2-} concentrations obtained by the MATCH model (ECLAIRE data set, period 1900-2020, 50 km resolution) [3] matches well the ice core data with the maximum in the 1970s (Fig 1). Absolute model concentrations are factor 6-8 higher than the ice core values and a factor of ~ 3 between CDD and the other sites is observed (Figs. 1,2, Tab. 1).

Due to the low resolution of the ECLAIRE dataset, the mean heights of the grids including the drilling sites are

between 1600 and 1800 m asl, far lower than their actual heights of 3900-4450 m asl. Typically, pollution concentrations in precipitation at lower altitudes are higher, due to the proximity to the sources. To test, whether the model output is influenced by the mean height of the Alpine grid cells, we additionally applied the MATCH model (BIODIV data set, period 1990-1999) [4] with a finer resolution (12 km). Here, the mean height of the grids representing the ice core sites span 2400 to 2700 m asl. Indeed, exSO_4^{2-} concentrations obtained from the BIODIV dataset are significantly lower compared to ECLAIRE, and are comparable to the ice core concentrations (Fig. 2b,c, Tab. 1). Furthermore, the BIODIV concentrations are similar for all 4 sites supporting the assumption of the same source regions of pollutants. Thus, the factor of ~ 3 between CDD and CG /FH/GG concentrations obtained from the ECLAIRE dataset may be caused by the influence of differing local surface concentrations at lower altitudes.

Tab. 1: exSO_4^{2-} concentrations in 10-year periods from ice cores and the ECLAIRE and BIODIV datasets.

exSO_4^{2-} ($\mu\text{g/l}$)	Ice core 1970-79	ECLAIRE 1970-79	Ice core 1990-99	ECLAIRE 1990-99	BIODIV 1990-99
CG	827	7257	524	4113	696
GG	876	7257		4113	696
FH	743	5188		2889	696
CDD	381	2311	285	1291	672

We conclude that the results of the BIODIV dataset better reflect absolute levels of concentrations at high-Alpine sites. However, small-scale processes such as wind erosion or locally varying importance of different seasonal precipitation leading to the observed differences at high-Alpine sites are not resolved in this model.

- [1] A. Eichler et al., this report, pp. 21.
- [2] D. Wagenbach et al., Geografiska Annaler A, Phys. Geogr. **94**, 245 (2012).
- [3] M. Engardt et al., Tellus B, **69**, 1 (2017).
- [4] BioDiv-Support, funded through the 2017-2018 Belmont Forum and BiodivERsA joint call for research proposals, under the BiodivScen ERA-Net COFUND program.

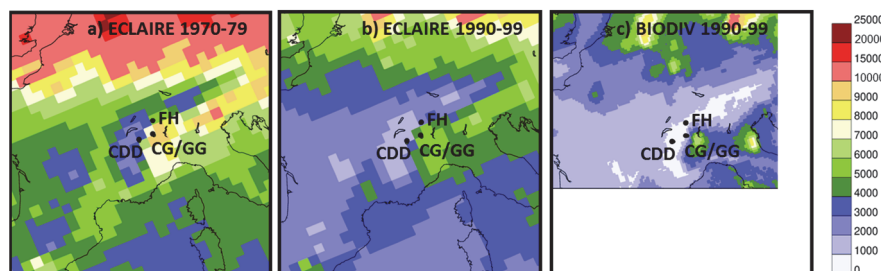


Fig. 2: Comparison of spatial exSO_4^{2-} concentrations in precipitation at the surface ($\mu\text{g/l}$) obtained by the MATCH model (a) ECLAIRE 1970-79, b) ECLAIRE 1990-99, c) BIODIV 1990-99). Ice core sites are marked.

THE ICE MEMORY PROGRAM

M. Schwikowski (PSI & Univ. Bern), C. Barbante (Univ. Venice), J. Chappellaz (IPEV), P. Ginot (IRD/IGE), A.-C. Ohlmann (FUGA)

As an international initiative, ICE MEMORY aims at collecting heritage ice cores from the world's key endangered glaciers to store them under safe conditions and international governance in Antarctica for future generations of scientists.

Mountain glaciers in the mid-latitudes and the tropics have dramatically retreated and thinned in recent times and are in danger of disappearing rapidly in the coming decades as global temperatures rise caused by anthropogenic emissions of greenhouse gases [1]. Not only the glacier termini are affected, but also the accumulation zones in the upper parts of the glaciers, where ice cores for paleo studies are collected. When there is absence of accumulation or even melting at the ice core sites, the age of the surface is no longer known, which is an important anchor point for dating, and the overlap with instrumental observations becomes shorter or non-existent [2]. Such an overlap is a fundamental prerequisite for calibrating subsequent ice core reconstructions. This is a major challenge the scientific community is facing, since glacial-archived information forming one of the best libraries of past climatic and environmental changes is under threat of being lost forever. Iconic examples are the plateau ice fields on Kilimanjaro in Africa, forming the largest ice body on that continent, which have experienced an area shrinkage of 85% between 1912 and 2000 [3]. The Quelccaya ice cap in the Peruvian Andes, where ice cores were collected already in 1983, showed, when re-drilled in 2003, the irreversible obliteration of the environmental signal in the top part due to unprecedented meltwater percolation through the firn portion during the last two decades [4].

As an international initiative, ICE MEMORY (IM) aims at collecting heritage ice cores from the world's key endangered glaciers. By creating an international ice core repository in Antarctica (Fig. 1), the heritage cores will be stored under safe conditions and under international governance, to provide high-quality samples for ice core science to be conducted by future generations of scientists throughout the world. For site selection, priority will be given to glaciers, whose scientific potential has already been proven through projects and publications independent from the IM project, and where good dating and glaciological information exist. The aim is to collect at least two parallel cores: one heritage and one reference core. The reference core will be analyzed for a maximum number of parameters with currently available technologies and the resulting data will be made available to the scientific community through an open data repository. Finally, a sustainable governance system in charge of managing the ice and data archives will be installed.

Since 2015, when ICE MEMORY evolved from a Franco-Italian initiative, which was joined by Switzerland in 2016, it has developed towards an international dimension under the patronage of UNESCO in 2017. Meanwhile five ice core drilling missions have been conducted in the frame of the project, at Col du Dôme, Mt. Blanc, France (2016), Illimani, Bolivia (2017), Belukha, Siberian Altai, Russia (2018), Elbrus, Caucasus, Russia (2018), and Grand Combin, Switzerland (2020). Drilling on Grand Combin showed that this glacier is already in such a delicate state, that the last two hot summers were sufficient to damage it forever ([5], [6], cover page).

Finally, on January 18th, 2021, the international Ice Memory Foundation was created. Under the auspices of University Grenoble Alpes Foundation, the shelter agreement was signed by the heads of the seven founding partners: French National Centre for Scientific Research, French National Research Institute for the Sustainable Development, French Polar Institute Paul-Émile Victor, National Research Council of Italy, Paul Scherrer Institute, University Ca' Foscari of Venice, University Grenoble Alps.

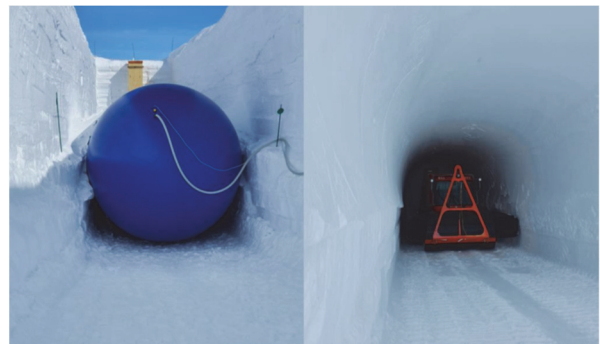


Fig. 1: Testing of the balloon technique to create the ice cave for long-term storage of the IM ice cores at Concordia station in Antarctica, coordinated by the Italian PNRA program with help from the French polar institute (photos courtesy of Rocco Ascione, PNRA/IPEV).

-
- [1] IPCC, *Climate Change 2013*, Cambridge University Press (2013).
 - [2] D. Zhang et al., *Environ. Sci. Technol.*, **49**, 9499–9500 (2015).
 - [3] N. Cullen et al., *The Cryosphere*, **7**, 419–431 (2013).
 - [4] L. Thompson et al., *Ann. Glaciol.*, **52**, 23–34 (2011).
 - [5] T. M. Jenk et al., this report, pp. 24.
 - [6] C. J. Huber et al., this report, pp. 25.

ICE CORE DRILLING ON GRAND COMBIN IN TIMES OF A WARMING CLIMATE

T. M. Jenk (PSI), J. Gabrieli, F. de Blasi, F. Dallo (CNR-ISP), C. Barbante, R. Lodi (CNR-ISP & Univ. Venice), P. Conz (Dolomiti Guides), R. Selvatico (Areaphoto), T. Singer, M. Schwikowski (PSI & Univ. Bern)

The attempt to save an ice core from Grand Combin (GC), providing a natural archive of European climate and pollution history for future generations, came too late. Recent climate warming not just visibly reshapes the glaciated landscape of the Alps, but also destroys its last ice archives at a fast rate.

From 13-21 September 2020, an ice core drilling campaign was conducted on the summit plateau of Corbasriere glacier, in the saddle of GC characterized by low slope and ice flow (Fig. 1a-c and cover page). Within the framework of ICE MEMORY [1], retrieval of three parallel cores to bedrock was aspired. While two of the cores were intended for immediate analysis as a reference (one each by PSI and University Ca' Foscari), the third was designated for storage in the planned ICE MEMORY repository in Antarctica [1].

In 2018, a reconnaissance campaign delivered ground penetrating radar measurements (Fig. 1c, d), and shallow coring confirmed signal preservation and yielded annual net accumulation rates [2]. This allowed selecting the most promising location for coring to bedrock.

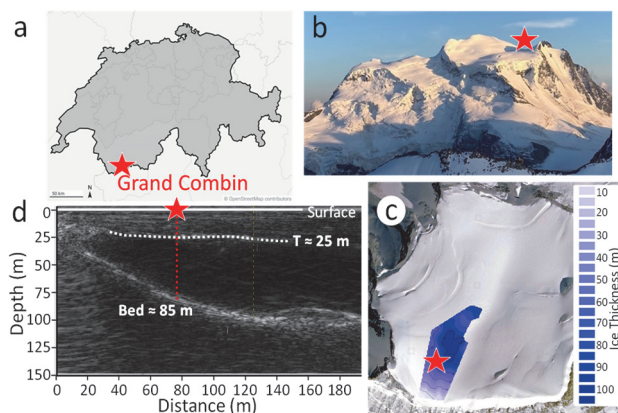


Fig. 1: GC drill site. (a) Map of Switzerland. (b) GC with its glaciated high plateau. (c) Plateau from above. Saddle highlighted by the radar derived ice thickness. (d) Radar profile. N-S transect with reflections of bedrock (Bed) and bottom of firn-ice transition (T).

In the early morning of 13 September, about 2000 kg of equipment and eight persons were flown to the drill site using eight helicopter rotations. Despite the high altitude (4100 m asl.), set-up of camp and drilling device was fast and completed by the evening. On day 2, drilling started smooth (7.29249 E, 45.93775 N, 4124 m), but thick ice lenses were already observed just a few meters into the firn (Fig. 2). With depth, drilling became troublesome. When pulled up, the drill often got stuck underneath certain thick ice layers. A problem so far never encountered elsewhere. At ~14 m depth, firn cores, were soaked with water, likely from surface melt and subsequent sub-surface run-off at the firn-ice transition (Fig. 1d). Once the motor (installed on top of the

drill) reached position of this soggy layer, the anti-torque system lost resistance and motor, instead of the cutting-ring, started spinning in the hole. Drilling became impossible and the drill got stuck below the ice layer on top of the watery stratum, possibly due to a small break-in of the borehole. In the morning of day 3, the drill had to be released by the use of anti-freeze. With this contamination, the borehole was lost (length core 1, 25.34 m). Also, drill motor and cable were seriously damaged from spinning. In a major effort on day 4, the drill was shipped to the manufacturer (~200 km away, icedrill.ch). It was fixed and again operational back in camp within < 24 h. In a new borehole (1.5 m away, 7.29251 E, 45.93774 N, 4124 m), drilling problems recurred at similar depths, despite reducing working to hours of colder temperatures. Finally, the drill had again to be released with anti-freeze (core 2, 17.57 m). The drill site was moved (20 m NNE) and a third borehole started (7.29265 E, 45.93781 N, 4122 m). Again only working when cooler, the borehole was now rimmed each run when passing depths of critical layers. This slowed down drilling, but allowed reaching final depth of borehole 2 without major problems. However, soon after, the drill got stuck again (core 3, 18.13 m). This time, release was successful without anti-freeze (~2 h). However, with no realistic chance to reach bedrock, a high risk of losing the drill and predicted bad weather, camp was taken down. Early on 21 September, the last persons and material flew out just minutes before clouds from the S covered the site, bringing one week of bad weather with no chance for evacuation by helicopter. First results from core 1 are presented in [2].



Fig. 2: Left: With glacier melting, smooth drilling at Grand Combin was rather an exception in 2020. Right: Firn core with thick ice lenses from refrozen surface meltwater.

We acknowledge funding from the Italian Ministry of Education, University and Research within the frame of the ICE MEMORY project.

- [1] M. Schwikowski et al., this report, pp. 23.
[2] C. J. Huber et al., this report, pp. 25.

MELTING INFLUENCED SIGNAL PRESERVATION AT GRAND COMBIN GLACIER

C. J. Huber (PSI & Univ. Bern), A. Eichler, S. Brüttsch, T. M. Jenk (PSI), J. Gabrieli, C. Barbante (Univ. Venice), M. Schwikowski (PSI & Univ. Bern)

An ice core from Grand Combin glacier showed influence of melting on major ion concentrations caused by recent warming. The signal seems undisturbed in the upper part, corresponding to the period 2016-2020, whereas some of the ions are largely depleted in the lower part (2008-2015). This opens the opportunity to investigate the effect of melting on organic tracers.

High-alpine ice cores serve as natural archives and allow access to pollution records back to the pre-industrial era. Because of global warming these environmental archives are in danger of experiencing melting and thus altering the information stored in glacier ice. A study by Eichler et al. [1] on an ice core from the Grenzgletscher showed diverse effects on concentrations of different major ions due to melting. In this work, we analysed an ice core collected on Grand Combin, Switzerland, in September 2020 [2], aiming at dating the core and assessing the effect of melting on signal preservation. In a second step, organic aerosol tracers will be determined in this core as part of the SNF Project “Organics in ice”. Therefore, we cut the core as close to the drilling date as possible to reduce contamination from storage in plastic tubes. The ice core was dated applying annual layer counting using water stable isotopes ($\delta^{18}\text{O}$) and concentrations of major ions (e.g. ammonium (NH_4^+)). The obtained $\delta^{18}\text{O}$ record shows excellent agreement with the record from a shallow core collected in a reconnaissance study in 2018 [2] for the overlapping period (2011-2018, Fig. 1a). However, when looking at the different major ion concentrations, we observe effects of melting before 2016. Fluoride (F^-) for example maintains annual cycles, albeit the cycles are less pronounced in comparison with the 2018 record (Fig. 1 b). As extreme case, sulfate (SO_4^{2-}) is significantly depleted from 2016 to 2008 (Fig. 1 d). Further, there are major ions such as magnesium (Mg^{2+}), which are also affected by melting but not as strongly as sulfate (Fig. 1 c). In addition, we calculated the concentration ratios between the part affected by melting (2008-2015) and the part we assume is not affected (2016-2020). In accordance to these ratios, we propose an elution sequence: $\text{CH}_3\text{SO}_3^- > \text{C}_2\text{O}_4^{2-} \approx \text{Ca}^{2+} \approx \text{SO}_4^{2-} > \text{NO}_3^- \approx \text{Mg}^{2+} > \text{F}^- \approx \text{NH}_4^+$. This agrees with the finding, that ammonium and fluoride, both having a high solubility in ice, are incorporated into the ice lattice, and therefore remain in the ice matrix even during melting [3,4]. In contrast, sulfate and calcium (Ca^{2+}) are enriched on ice crystal surfaces and are therefore prone to depletion under melting events [3,4]. All sea salt species (potassium (K^+), sodium (Na^+), chloride (Cl^-)) were excluded from the discussion, since we observed so far unexplained discrepancies between the concentrations measured in the meltwater unaffected part of the two cores.

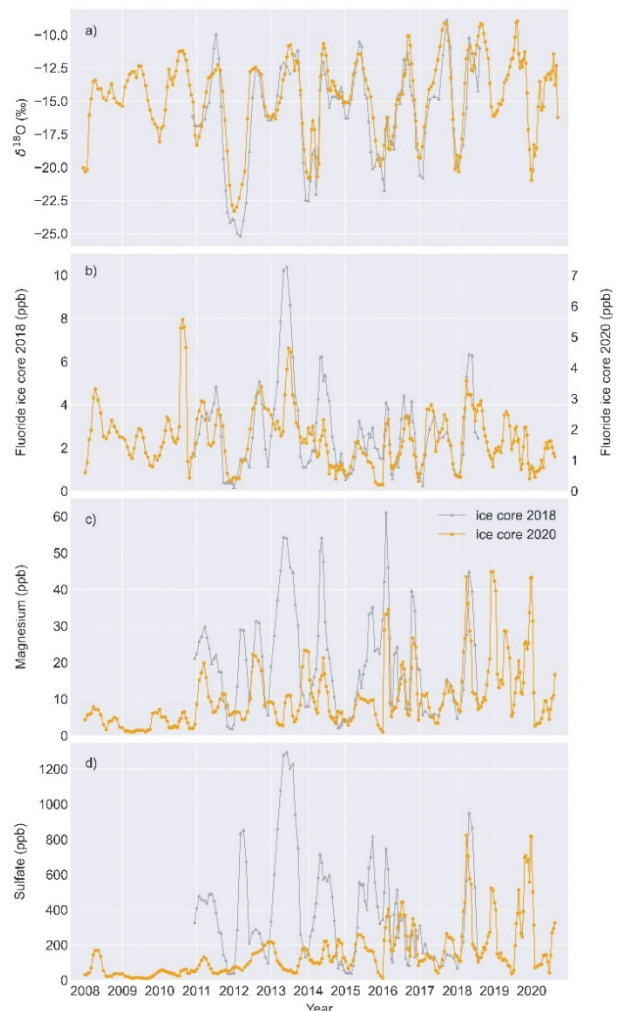


Fig. 1: Comparison of records from the two ice cores drilled at Grand Combin Glacier in 2018 and 2020: a) $\delta^{18}\text{O}$, b), c), and d) concentrations of fluoride, magnesium, and sulfate are shown.

We acknowledge funding from the Swiss National Science Foundation (Grant 200021_182765). We would like to thank the ice core drilling team. Ice core drilling was funded by the Italian Ministry of Education, University and Research.

- [1] A. Eichler et al., *Tellus*, **53B**, 192-203 (2001).
- [2] T. M. Jenk et al., this report, pp. 24
- [3] S. E. Avak et al., *J. Geophys. Res. Earth Surf.*, **124**, 1647-1657 (2019).
- [4] J. C. Trachsel et al., *Front. Earth Sci.*, **7**, 1-19 (2019).

CARBONACEOUS AEROSOL RECORDS OF TWO ALPINE ICE CORES

T. Singer, L. Fang (PSI & Univ. Bern), T. M. Jenk (PSI), M. Schwikowski (PSI & Univ. Bern)

A carbonaceous aerosol record from Colle Gnifetti ice core is presented and compared to the record from nearby Fiescherhorn glacier (Swiss Alps). Overall they agree well with low concentrations during the pre-industrial period and a concentration increase in the 20th century.

Atmospheric aerosols are a topic of great interest because they influence the climate system both indirectly, through their interaction with clouds, and directly, through scattering and absorption of incoming solar radiation. In addition to their impact on climate, they also affect human health. An estimated 7 million people die each year from diseases such as stroke, heart disease and lung cancer caused by exposure to particulate matter in polluted air [1]. Carbonaceous aerosols are the dominant component of atmospheric aerosols and account for roughly 40% of the total aerosol mass [2]. They consist of two major fractions, elemental carbon (EC; also denoted as black carbon, BC) and organic carbon (OC). Based on its solubility, OC is further divided into water-insoluble organic carbon (WIOC) and water-soluble organic carbon (WSOC). Unlike WIOC, which mainly consists of primary organic aerosol from direct emissions (e.g. plant and soil debris, fuel combustion, biomass burning), WSOC is largely related to secondary organic aerosols (SOA) formed in the atmosphere from volatile organic precursors [3]. To date, the sources of WSOC are not well-constrained. Natural archives such as ice sheets and glaciers contain valuable information about the history of the Earth's atmosphere. High alpine ice cores are of particular interest, as they are surrounded by densely populated and highly industrialised regions undergoing strong changes due to human activities (e.g. aerosol emissions from the combustion of fossil fuels).

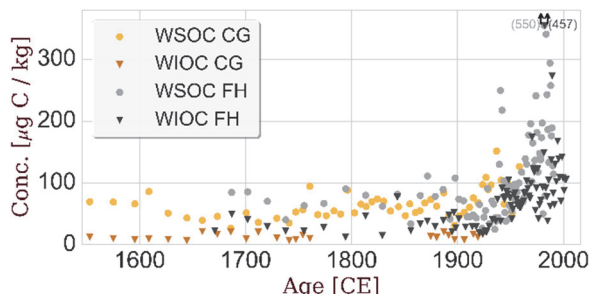


Fig. 1: WSOC and WIOC concentration records from the CG and FH ice cores.

Dissolved organic carbon (DOC) and WIOC concentrations were analyzed in an ice core from Colle Gnifetti (CG, 4455 m a.s.l.) using the methods in [4] and [5]. From DOC, WSOC can be derived by subtracting the most abundant monoacids, i.e. formate and acetate. In Fig. 1, the new ice core records of WIOC and WSOC

from Colle Gnifetti are compared to the respective, existing records from Fiescherhorn (FH, 3900 m a.s.l.) [5]. These records cover both, the preindustrial (PI) and industrial period (I), crucial to assess the anthropogenic impact on atmospheric pollution and potential effects on climate. While the record from FH is complete (continuous from 1680-1990 for WSOC and from 1680-2002 for WIOC), analysis of the CG ice core is work in progress and the record currently discontinuous, so far covering time periods between 1545 and 1950 (preliminary data). Consistent with the records from CG and FH, we observe OC concentration levels to remain rather constant between 1545 and 1900, with WSOC concentrations generally being higher by around a factor of 5 ± 1.9 for CG (1545-1900) and 2.7 ± 1.1 for FH (1680-1900). The most striking feature of the FH record is the sharp increase at about 1940 [5]. Interestingly, PI OC, especially WIOC concentrations, are generally lower at the CG than at the FH. This might be related to the difference in altitude of the two sites, with the CG being higher and thus the vertical transport of atmospheric aerosol (particularly of primary particles) to this location being more restricted. Also consistent is an increase in OC observed in the 20th century in both ice cores (only WSOC available for CG yet). The mean values for the PI and I are summarised in Tab. 1, showing increased levels in I, clearly reflecting the impact of anthropogenic emissions.

Tab. 1: Mean WSOC and WIOC concentrations and their ratio for CG and FH (\pm standard deviation). A distinction is made between the PI and I period.

Period	Site	WSOC [$\mu\text{gC kg}^{-1}$]	WIOC [$\mu\text{gC kg}^{-1}$]	WSOC/WIOC ratio
PI	FH	72 ± 15	32 ± 17	2.9 ± 1.4
	FH	72 ± 15	31 ± 10	2.2 ± 0.4
	CG	55 ± 16	12 ± 5	5 ± 2.2
I	CG	56 ± 16	12 ± 5	5 ± 2.2
	FH	94 ± 63	54 ± 39	2 ± 0.9
	CG	73 ± 36	33 ± 7	2.2 ± 0.7
		72 ± 26	13 ± 4	4.9 ± 1.2

1680-1850, 1680-1760, 1545-1850, 1545-1760, 1850-1990, 1850-1950, 1870-1920

We acknowledge funding from the Swiss National Science Foundation (Grant 200021_182765).

- [1] World Health Organization. Global Ambient Air Quality Database (2018).
- [2] K. E. Yttri, European Monitoring and Evaluation Programme EMEP (2007).
- [3] A. Gelencsér et al., *J. Geophys. Res.* **112** (2007).
- [4] C. Uglietti et al., *The Cryosp.* **10**, 3091-3105 (2016).
- [5] L. Fang et al., *Radiocarbon*, **61**, 681-694 (2019).

METHOD FOR DETERMINING ORGANIC FIRE TRACERS IN ICE CORES

F. Burgay (PSI), D. Salionov (PSI LBK), A. Eichler (PSI), T. Singer, C. J. Huber (PSI & Univ. Bern), S. Bjelic (PSI LBK), M. Schwikowski (PSI & Univ. Bern)

A mass spectrometric method based on liquid chromatography after solid phase extraction (SPE-LC-MS) was designed and optimized for the determination of organic wildfire tracers in ice cores.

Biomass burning fires are a significant source of organic aerosols into the atmosphere since they contribute up to 39% of the particulate organic carbon [1]. Their frequency and extension have dramatically increased in recent years [2], posing an environmental threat mainly at high latitudes where they contribute to the progressive melting of permafrost and the potential release of greenhouse gases into the atmosphere [3].

Evaluation of how wildfires can affect the climate system and a reconstruction of their past regional and temporal variability over the last millennia is required. Ice cores represent the most reliable archive to perform palaeofire reconstructions since they can provide a precise chronology and a close connection with the past climate conditions [4]. To date, mainly inorganic proxies are used; however, since biomass burning particles are constituted by a wide range of organic molecules [1], the identification and evaluation of wildfire organic tracers represents the new frontier in ice core science. Several studies have been performed on selected molecules such as levoglucosan and aromatic compounds [4]. In this study, we present an optimization of a previous method [5] for the determination of five organic biomass burning markers: syringic acid (SA), vanillic acid (VA), syringaldehyde (SYA), p-hydroxybenzoic acid (PHA) and pinic acid (PA) (Fig. 1).

The method was optimized from both the instrumental and operational point of view. All the analyses were performed using a high-resolution hybrid quadrupole-Orbitrap mass spectrometer in negative ionization mode (Q Exactive Focus, Thermo Fisher Scientific), coupled with an Ultra High-Performance Liquid Chromatography system (Ultimate 3000, Thermo Fisher Scientific).

We achieved low limits of detection and excellent trueness values by optimizing both chromatography and mass spectrometry parameters. In details, the external linear calibration curves (from 0.1 ng g^{-1} to 3 ng g^{-1}) had an $R^2 \geq 0.99$ for all the compounds. The instrumental LoD were 1.6 pg (SA), 4.1 pg (VA), 1.6 pg (SYA), 2.9 pg (PHA) and 3.8 pg (PA). Trueness (O/T %), defined as the ratio between the obtained concentration (O) and the true concentration (T), was evaluated using quality control samples at 0.5 and 1 ng g^{-1} and ranged between 86% and 117%, depending on the molecule.

The targeted biomass burning tracers are present in ice core samples at a pg g^{-1} level or lower [6]. Thus, a pre-concentration step is required to enhance the signal-to-noise ratios of the targeted compounds. A Solid Phase

Extraction (SPE) step was then included in our procedure. Water samples ($n = 5$) spiked with a known amount of the compound mixture (final concentration = 30 pg g^{-1}) were loaded and then eluted on a Strong Anion Exchange (MAX) cartridge after proper conditioning, decontamination and counter ion exchange steps. Taking into account the pre-concentration efficiency and the sample loading volume (50 mL), the procedural detection limits were 10 pg g^{-1} (SA), 8 pg g^{-1} (VA), 10 pg g^{-1} (SYA), 20 pg g^{-1} (PHA) and 20 pg g^{-1} (PA). Reproducibility was between 3 and 10% RSD, while recovery ranged between 40 and 90% at 30 pg g^{-1} concentration level.

This method will be applied to both European and Siberian ice cores to provide useful insights into the past fire activities in these regions over the last centuries. The analysis will be coupled with an untargeted approach in order to identify other organic aerosol markers. Lastly, this method will also be applied on snow and firn matrices to evaluate the stability and preservation of these species in real environmental samples, enabling a more quantitative interpretation of the ice core records and a better understanding of the link between these tracers and the past climate conditions.

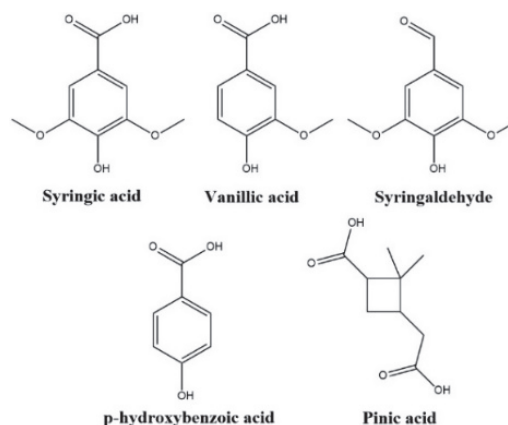


Fig. 1: The targeted wildfire tracers.

We acknowledge funding from the Swiss National Science Foundation (Grant 200021_182765).

- [1] K. Kawamura et al., *Geochim. Cosmochim. Acta*, **99** (2012).
- [2] Copernicus Atmosphere Monitoring Service, ECMWF.
- [3] G. Hugelius et al., *PNAS*, **117**, 34 (2020).
- [4] M. Legrand et al., *Clim. Past.*, **12**, 10 (2016).
- [5] A. Vogel et al. *Environ. Sci. Technol.*, **53**, 21 (2019).
- [6] A. King et al., *Anal. Chem.* **91**, 8 (2019).

ANALYSIS OF FIRE TRACERS IN ICE CORES

J. Stoll, M. Schwikowski (PSI & Univ. Bern), F. Burgay, A. Eichler (PSI), D. Salionov, S. Bjelic (PSI LBK)

An LC-MS method for the simultaneous detection of structurally different biomass burning tracers is developed. The use of LC-MS allows avoiding additional steps that are prone to sample loss or contamination and requires large sample volume (e.g. derivatization).

Biomass burning includes not only natural forest fires but also slash- and burn of forests so that the area can be used for agriculture. These fire events release different compound classes to the atmosphere, (e.g. greenhouse gases, black carbon, organic compounds) that interfere with the earth's climate, by altering the earth's radiative forcing and human health. It is therefore of big interest to identify and describe compounds released during fire events. Ice cores operate as climate archives: Information about past fire events can be reconstructed as molecules released to the atmosphere will be deposited with snow or by dry deposition. [1]

For this study, the three biomass burning tracers (bb tracers) levoglucosan, vanillic acid and p- hydroxybenzoic acid were chosen to develop a method for their simultaneous detection and quantification through Liquid Chromatography-High Resolution Mass Spectrometry (LC-HRMS) analysis. A major challenge during this work was to find a method that is suitable for the different compound classes, phenolic acids (vanillic acid and p- hydroxybenzoic acid) and anhydrous sugar (levoglucosan) (Fig.1). All three tracers are pyrolysis products of the wooden part of plant material; the phenolic acids are formed during pyrolysis of lignin and levoglucosan when pyrolysing of cellulose. The similarity in source leads to a similarity in ice core profile. [2]

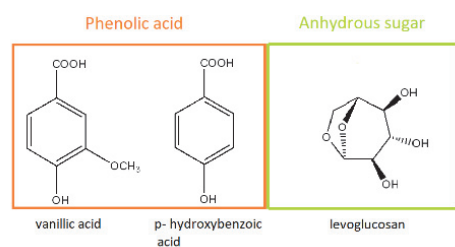


Fig. 1: Molecular structure of the biomass burning tracers considered in this study.

Levoglucosan likely forms adduct ions with ammonium in positive ion mode [3]. Phenolic acids on the other hand, are commonly measured in the negative ion mode [4].

In the first part of the project, the ionization efficiency of all three compounds was improved. This was done by testing the different additives ($(\text{NH}_4)_2\text{CO}_3$, $\text{NH}_4\text{CH}_3\text{CO}_2$, NH_4HCO_3 , NH_4HCO_2 , NH_4F , AgCl and H_2CO_2 : 5mM solutions of additives were dissolved in solutions (0.01 mg mL^{-1}) containing one of the biomass

burning tracers. The samples were analyzed via direct injection using Electro Spray- Ionization (ESI-MS) in negative and positive ion mode. The peak intensity was determined using the software Xcalibur.

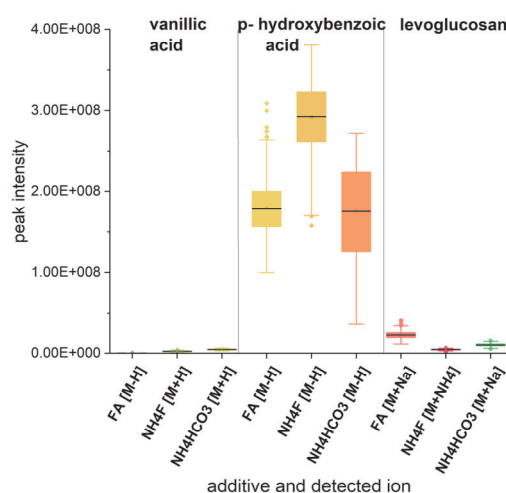


Fig. 2: Boxplot showing intensities of the [M-H] ion for different additives, obtained by multiplication of the individual peak intensity of all three bb tracers. The [M-H] ion was selected as most intense one for all additives.

AgCl produced the highest peak intensity. However, the signal was not stable. This might be caused by the low solubility of AgCl (1.9 mg L^{-1} at 25° in water). The second best additive is NH_4HCO_3 (Fig.2). For reproducible data, we need a stable and intense signal. For this reason, the more soluble AgNO_3 (2.16 g L^{-1} at 20° in water) will be tested in a further step.

We acknowledge funding from the Swiss National Science Foundation (Grant 200021_182765).

- [1] H. Bhattarai et al., *Atmos. Res.*, **220**, 20-33 (2019).
- [2] K. Kawamura et al., *Geochim. Cosmochim. Acta*, **99**, 317-329 (2012).
- [3] E. Wan et al., *J. Chromatogr. A*, **1107**, 175-181 (2006).
- [4] X. Wan et al., *Environ. Pollut.*, **247**, 216-218 (2019).

THE DIFFICULTY OF ALIQUOTING ICE CORE SAMPLES

T. S. Münster (PSI & Univ. Bern), T. M. Jenk (PSI), C. J. Huber (PSI & Univ. Bern), A. Eichler (PSI), P. Nalivaika (PSI & Univ. Bern), M. Schwikowski (PSI & Univ. Bern)

The availability of similar, homogenous sampling material is a prerequisite when aiming to thoroughly compare different analytical setups. Since melted ice samples are colloids, containing dispersed insoluble particles, obtaining such aliquots is particular challenging.

In order to investigate comparability of two different mass spectrometer (MS) setups, designed for the analysis of trace elements (TE) in ice, the best approach to obtain aliquots of glacier ice samples was tested. They are aimed to compare the analytical performance between the inductively coupled sector field (ICP-SF)-MS system at PSI currently in use for TE analysis in ice cores, and a new ICP-Time Of Flight (TOF)-MS system at the University of Bern. The benefit of the ICP-TOF-MS is, it's much faster in mass scan, allowing analysis of single particle composition required for a better allocation of the source of mineral dust deposited on the glacier. This is of interest, because changes in these sources can then potentially be reconstructed using ice cores as natural archives of the past, allowing insight into temporal changes of atmospheric circulation patterns. In this study, the best approach and potential limitations for obtaining aliquots of ice samples was investigated. Since single particle analysis is a major goal, a complete dissolution of particles needs to be avoided. This significantly increases the challenge for aliquoting because of the inhomogeneous nature of the sample. The test here was performed with six samples of the Cerro Negro core (Chilean Andes, 4604 m asl.), acidified to 0.2 M with suprapure 68% HNO₃ and analysed with the PSI ICP-SF-MS.

The following experiment was performed to check for the potential introduction of a concentration bias by the aliquoting procedure. On day one, the initial ice samples (A) were melted and 1/3 of the volume was transferred to aliquots B and C. Aliquot C was immediately refrozen without additional treatment. Aliquots B and three of the samples A were analysed after being acidified for a defined reaction time of 1.5 min. The leftover of aliquots B were immediately refrozen (acidified), simulating one possible way of transportation to Bern. On the second day, the remaining three aliquots of A and aliquots C were analysed (same acidification procedure as on day one). Also, aliquots B were re-analysed.

Significant differences in concentrations were observed between the respective samples A and their aliquots B and C (Fig. 1). While potential wall effects (i.e. the adsorption of TEs on the tube walls) seem improbable to cause such a large bias, we think it is caused by undissolved mineral dust particles. These particles remained predominantly in tube A (decanting of a suspension).

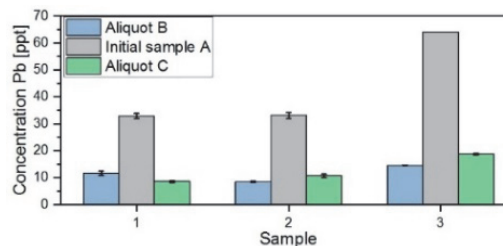


Fig. 1: Effect on Pb concentration caused by the two different aliquoting procedures tested. Each bar represents the mean of three replicate measurements, with the standard deviation shown by the error bar.

Because TEs from particles are leached into solution once the sample is acidified [1, 2], the higher number of particles in A compared to B and C, thus yielded a higher concentration in this fraction. Our experiment further indicates that refreezing of samples and subsequent storage does not cause a bias for untreated samples. However, samples being acidified prior to refreezing (with the aim to minimize potential wall effects), do show elevated concentrations (Fig. 2). This is likely explained by the time needed until the sample is frozen entirely. Until then, leaching of particles is ongoing and it is known that increasing the acidification time results in higher concentrations [1, 2]. Due to expelling of impurities from the ice while freezing, the effect is likely even enhanced by steadily increasing acid concentration in the non-frozen portion of the sample.

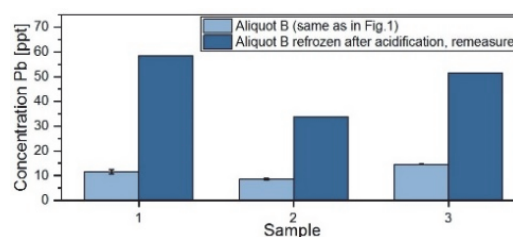


Fig. 2: Effect on the concentration of Pb for samples being melted and refrozen immediately after acidification.

This test illustrates that aliquots from natural ice samples cannot be obtained easily without introducing an artificial concentration bias, particularly for ice containing high concentrations of mineral dust like the Cerro Negro samples. Despite the expected uncertainty introduced by small scale inhomogeneity in glacier ice, an optimal comparability between the PSI and Bern MS systems can only be achieved by cutting parallel samples from identical depths of the ice core.

- [1] T. S. Münster et al., LUC Annual Report, 33 (2019).
- [2] R. H. Rhodes et al., Chem. Geol., 286, 207-221 (2011).

ALBEDO REDUCTION AND ENHANCED MELT RATES OF OLIVARES GLACIERS

M. Barandun (PSI & Univ. Fribourg), A. Rivera (Univ. Chile), C. Bravo (Univ. Leeds), B. Grobety (Univ. Fribourg), L. Fang (PSI), S. Köchli (PSI), T. S. Münster (PSI & Univ. Bern), K. Naegeli (Univ. Bern), S. Cisternas (CECs), M. Schwikowski (PSI & Univ. Bern)

Glaciers in the Olivares basin, located in Central Chile, have lost mass at an above-average rate in Chile since the beginning of the 1980's. So far, it is not clear why these glaciers respond with such an enhanced mass loss in comparison to their neighboring glaciers. Here, we investigate natural and anthropogenic induced processes, which may have led to increased glacier melt rates over the past decades.

The glaciers situated in the Olivares basin, Central Chile, show an increase of mass loss of roughly -0.28 m w.e. yr^{-1} from 1980 to 2000 to -0.32 m w.e. yr^{-1} from 2000 to 2018 [1, 2]. For the latter period, glacier mass loss was twice as high as the average of the surrounding catchments [2], and is especially pronounced for the glaciers Olivares Alfa (-0.85 m w.e. yr^{-1}) and Paloma Norte (-0.97 m w.e. yr^{-1}) [1]. The increased mass loss might be related to a lowering of the surface albedo [3], and a link between albedo loss and mobilization of dust particles through mining activity was suggested [3]. Many glaciers of the Olivares basin have shown a significant negative trend in ice albedo since 1986 [3]. However, the cause of the decreasing albedo trend is so far unclear, and no conclusive evidence can relate anthropogenic activities nor the observed albedo changes with the enhanced melt rates [3]. Here, we investigate the possible causes of changing surface albedo and the sensitivity of the glacier mass balance to sub-seasonal albedo changes of the basin.

Our approach includes multiscale and multisource analyses. It combines for the first time microscopic, in situ and satellite-based surveys with mass balance modeling of the Olivares glaciers. We use end-of-summer Landsat satellite images to calculate ice albedo trends from 2000 to 2018 [4] and sub-seasonal albedo maps from 2013 to 2018 to monitor winter snow depletion patterns and snow albedo changes. The satellite-based albedo observations are related to in-situ and laboratory measurements to reveal the chemical and mineralogical composition of light absorbing impurities deposited at the glaciers surface in recent years (surface samples) and back to approximately the 1930s (ice core samples).

The ice albedo of the Olivares glaciers has decreased by 0.14 per decade from 2000 to 2018. This trend is only slightly more negative than for the surrounding basins. However, an essential factor for the negative mass balance is probably the pronounced snow albedo reduction at the end of the winter (Fig. 1). The snow albedo for Olivares Alfa and Paloma Norte dropped strongly already early in the season. Hence, the winter snow depletes faster and the ice surface is exposed to the atmosphere during a longer period in summer. This can cumulate to a significantly higher melt rate, due to lower albedo of ice surfaces in comparison to snow cover.

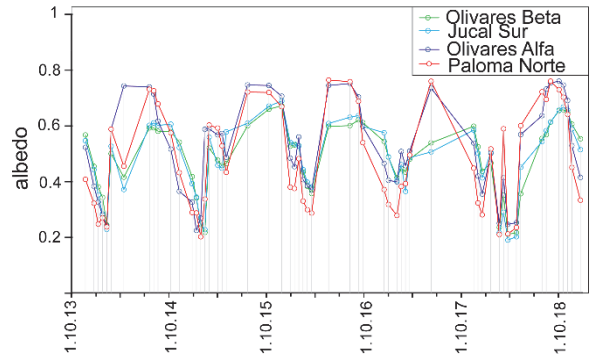


Fig. 1: Sub-seasonal snow albedo from 2013 to 2018 for four glaciers located in the Olivares basin.

The ice albedo in the region is typically reduced by the growth of penitents during the ablation period [5], by deposition of light absorbing impurities and by accumulation of liquid water at the surface. The snow albedo is reduced due to snow aging and deposited impurities.

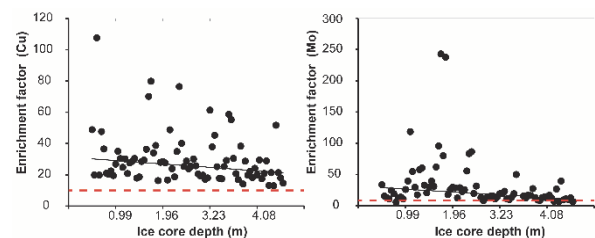


Fig. 2: Enrichment factors for Co and Mo concentrations measured in the ice core drilled in the basin. Values over 10 suggest anthropogenic pollution.

Dust particles deposited on the glaciers may be of anthropogenic origin as seen from a gradient of increasing occurrence of iron oxides and iron sulfides as well as enriched trace elements (Cu, Mo, Co and Pb) for sampling sites with greater proximity to a copper mine (i.e. Olivares Alfa, Paloma Norte). Enrichment factors for the same trace elements from element concentration in the ice core decreased with depth, and thus increased with time (Fig. 2). Iron oxides and copper containing pyrite have lower reflectance properties than silicates of the region. Together, it suggests an anthropogenic contribution to dust deposition and lowering of surface albedo, which could, however, so far not be quantified.

We acknowledge funding from the Centro de Estudios Científicos, Valdivia, Chile.

- [1] I. Dussaillant et al., *Nat. Geosci.*, **12**, 802 (2019).
- [2] D. Fariás-Barahona et al., *R. Sens.*, **12**, 1658, (2020).
- [3] T. E. Shaw et al., *J. Glac.*, **67**, 1 (2020).
- [4] K. Naegeli et al., *TC*, **13**, 397, (2019).
- [5] S. Lhermitte et al., *TC*, **8**, 1069 (2014).

CROSS DATING OF TWO BELUKHA ICE CORES

V. Wilson (PSI & ÅAU), A. Eichler, S. Brütsch (PSI), P. Nalivaika, T. Singer (PSI & Univ. Bern), T. Papina (IWEP), M. Schwikowski (PSI & Univ. Bern)

The 26.5 m uppermost part of a new Belukha ice core drilled in 2018 was dated using reference horizons and annual layer counting, revealing that the investigated segment covers the period 1985-2018.

An ice core from the Belukha glacier in the Siberian Altai drilled in 2001 (B01) was used to reconstruct temperature changes in the Siberian Altai, the history of biogenic emissions and forest fires from Siberian forests, past anthropogenic emissions of NH_3 , NO_x , SO_2 , and heavy metals from Eastern Europe/former Soviet Union (FSU) during the past 750 years (see e.g. [1]-[3]). To up-date the B01 core to the present and extend it from AD 1250 further back in time, a new 160 m deep core to the bedrock was collected from the Belukha glacier in 2018 (B18) [4]. The two major aims for investigating this new ice core are to reconstruct the pre-industrial to industrial changes of organic aerosols and the recent development of heavy metal emissions in the FSU.

The uppermost 26.5 m of the B18 ice core was sampled and analyzed as part of an internship at the PSI. The aim was to compare chemical records between the B18 and B01 ice cores, in order to cross-date the B18 ice core.

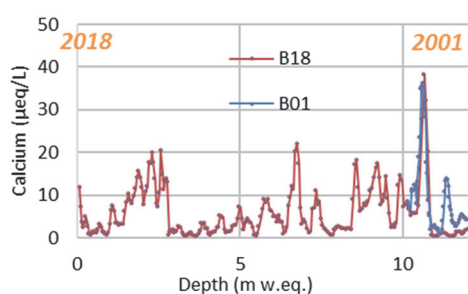


Fig. 1: Ca^{2+} concentrations in the upper 19.5 m (12 m w.e.) of the B18 core (red) and the onset of the B01 core at a depth of 10.1 m w.e. (blue). The two reference horizons 2001 and 2018 are shown in orange.

The upper 26.5 m (17 m w.e.) of the B18 core were sampled in the cold room of the PSI with a resolution of 8 cm and analyzed for major ions, water stable isotopes, and black carbon. Obtained records were compared with those from the well-dated B01 core. This way we could fix three “reference” horizons of known age in the B18 core:

- (1) year 2018 at 0 m w.e. (drilling date),
- (2) year 2001 at 10.1 m w.e. (onset B01 core in the B18 records based on Ca^{2+} , see Fig. 1),
- (3) year 1985 at 17 m w.e. (agreement in the B01 and B18 records of many species, not shown).

To determine the B18 age-depth scale in between the reference horizons we applied annual layer counting based on seasonal varying signals of selected species (see Fig. 2). For this, the software “Ice Core Dating” was used. Na^+ , NH_4^+ , Ca^{2+} , HCOO^- , SO_4^{2-} , and $\delta^{18}\text{O}$ records exhibit pronounced summer/winter variations in snow deposited on the glacier, which helped with the

annual layer identification (Fig. 2). For most of the ice core, clear annual layers could be seen, only in some parts of the ice core melting had occurred, complicating the dating (Fig. 2). Regardless, based on comparing various species we were able to establish an age-depth relation for the upper 26.5 m of the B18 core in the period 1985-2018. The resulting average annual accumulation rate of 0.51 m w.e. for the B18 core is in good agreement with that of the B01 core (0.56 m w.e.) [1].

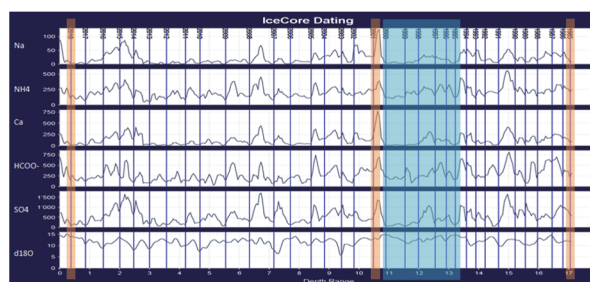


Fig. 2: Screenshot from the “Ice Core Dating” software. Records of Na^+ , NH_4^+ , Ca^{2+} , HCOO^- , SO_4^{2-} , and $\delta^{18}\text{O}$ in the upper 17 m w.e. of the B18 core are shown from top to bottom. Orange bars indicate the three reference horizons 2018 (left), 2001 (middle), and 1985 (right) and the dark blue vertical lines annual layers between 1985 and 2018. The light blue area highlights a part with signal smoothing due to an influence of melting.

Annual records of chemical species agree well between the B18 and B01 core (see e.g. NH_4^+ , Fig. 3), corroborating the established dating and allowing to update the B01 records to 2018.

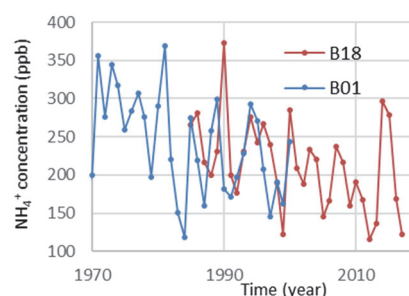


Fig. 3: Annual NH_4^+ concentrations for the B01 (blue) and B18 cores (red) in the period 1970-2018.

We acknowledge funding from the Swiss National Science Foundation (Sinergia, Grant 154450) and Swiss Polar Institute for ice core drilling.

- [1] S. Olivier et al., *J. Geophys. Res. Atmospheres*, **111**, D05309, doi:10.1029/2005JD005830 (2006).
- [2] A. Eichler et al., *Geophys. Res. Lett.*, **36** (2009).
- [3] A. Eichler et al., *ES&T*, **46**, 4323 (2012).
- [4] T. M. Jenk et al., *LUC Annual Report*, **2018**, 31 (2019).

CROSS-DATED ICE CORE RECORDS FROM THE TSAMBAGARAV GLACIER

P. Nalivaika, L. Marti, T. Singer (PSI & Univ. Bern), S. Brütsch, T. M. Jenk (PSI), T. Papina (IWEF), M. Schwikowski (PSI & Univ. Bern), A. Eichler (PSI)

Two parallel ice cores from the Tsambagarav glacier, Mongolian Altai, were cross-dated by comparing major ions and water stable isotope records. Exceptional agreement in the exSO_4^{2-} concentration records shows that this site is representative for SO_2 emissions of the former Soviet Union (FSU).

In 2009, two ice cores (72 m and 52 m length, distance few meters) were recovered from the Tsambagarav mountain range (Mongolian Altai). Whereas the 72 m core was previously studied and dated, covering the period 4800 BC-2009 AD [1], no age-depth scale has been obtained for the 52 m core so far. However, to use this latter core as an archive of recent heavy metal emissions from the former Soviet Union (FSU) [2], a precise dating is required.

Dating of the 52 m core was performed by synchronizing chemical records with those of the well-dated 72 m core using a specialized CoreMatch software [2]. Comparison of the records demonstrated an exceptional agreement for water stable isotopes ($\delta^{18}\text{O}$, δD) and anthropogenically derived species such as NH_4^+ , NO_3^- , and excess- SO_4^{2-} . The dating showed that the 52 m core covers the period 1710-2009 AD.

To evaluate the quality of the cross-dating we used annual exSO_4^{2-} records (non-dust SO_4^{2-}), calculated according to: $[\text{exSO}_4^{2-}] = [\text{SO}_4^{2-}] - 0.22 \cdot [\text{Ca}^{2+}]$. The pre-industrial $\text{SO}_4^{2-}/\text{Ca}^{2+}$ ratio of 0.22 agrees well with the ratio of 0.24 obtained for a Belukha ice core recovered from the Siberian Altai in 2001 [3], 350 km northwest from the Mongolian Altai site. Annual exSO_4^{2-} records between the two Tsambagarav cores correspond well, revealing consistent exSO_4^{2-} spikes following the volcanic eruptions of Laki (1783), Tambora (1815), and Katmai (1912) (Fig. 1). These volcanic horizons can be clearly distinguished from 5-year and 10-year concentration records (Fig. 2). An increase in exSO_4^{2-} concentrations in the second half of the 20th century (Figs. 1 and 2) is explained by a major anthropogenic source: SO_2 emissions from fossil fuel combustion.

5- and 10-year exSO_4^{2-} concentration records from the Mongolian Altai are well correlated with those of the Siberian Altai and with SO_2 emission estimates from the FSU (1750-2010). Correspondence is much better for the 10-year records, indicating that 5-year averages similar to 1-year means are not only influenced by the sources of air pollutants, but additionally by short-time fluctuations related to their transport to the high-altitude sites and post-depositional processes.

Thus, our study revealed that the 52 m Tsambagarav ice core covers the last ~300 years and is a representative archive for anthropogenic emissions from the FSU based on 10-year averages.

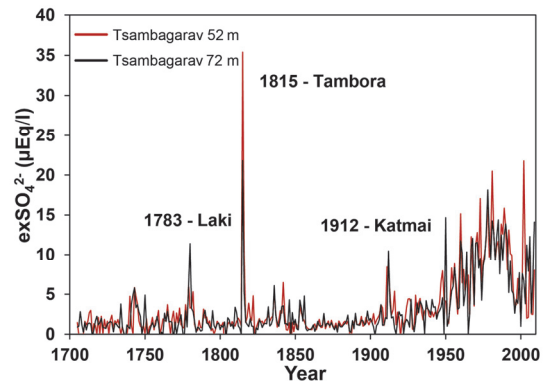


Fig. 1: Annual records of exSO_4^{2-} for the parallel 52 m and 72 m Tsambagarav ice cores.

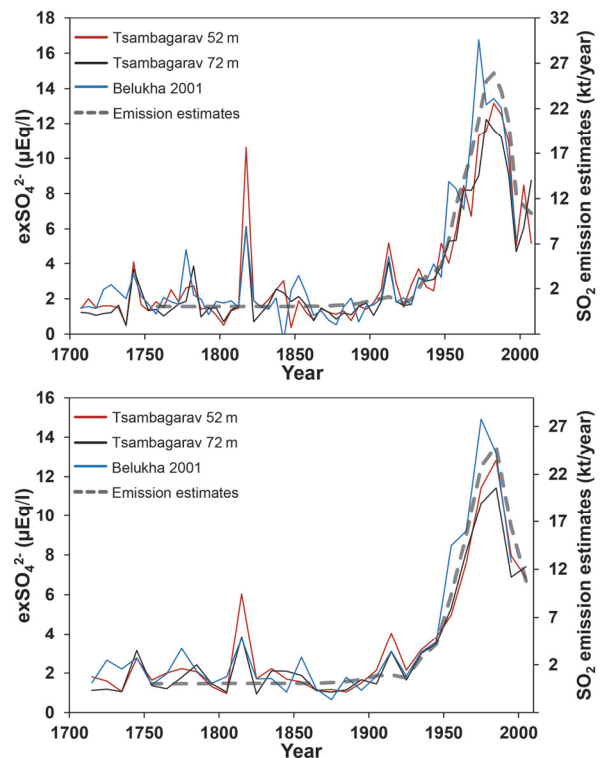


Fig. 2: 5-year (top) and 10-year (bottom) mean concentrations of exSO_4^{2-} for the 52 m, 72 m Tsambagarav ice cores; 2001 Belukha ice core and SO_2 emission estimates for the FSU territory (1750-2010 AD) [4].

We acknowledge funding from the Swiss National Science Foundation (Grant 181985).

- [1] P. A. Herren et al., *Quat. Sci. Rev.*, **69**, 59 (2013).
- [2] P. Nalivaika et al., *LUC Annual Report*, **2019**, 30 (2020).
- [3] S. Olivier, et al., *J. Geophys. Res.*, **111**, D05309, (2006).
- [4] R. M. Hoesly et al., *Geosci. Model Dev.*, **11**, 369 (2018).

FIRST Pb RECORD FROM THE TSAMBAGARAV ICE CORE

P. Nalivaika, T. S. Münster, M. Schwikowski (PSI & Univ. Bern), T. Papina (IWEF), T. M. Jenk, A. Eichler (PSI)

A 300-year ice core Pb record from the Tsambagarav glacier, Mongolian Altai, was used to investigate recent Pb pollution from the territory of the former Soviet Union (FSU). Our results show that recent Pb trends are strongly dependent on the applied dust correction to disentangle anthropogenic from natural Pb.

Anthropogenic pollution by lead (Pb) presents a serious concern because of its neurotoxic effect on humans. Anthropogenic Pb pollution sources include mining, metal smelting, waste incineration, coal and leaded gasoline combustion. Whereas recent Pb pollution is well documented in natural archives for many regions worldwide, existing Pb ice core records and expert emission estimates for the territory of the former Soviet Union (FSU) reveal an opposing trend in the recent ~30 years [1]. In order to resolve this discrepancy, an ice core from the Tsambagarav mountain range drilled in 2009 was analyzed, covering the period 1710-2009 AD [2].

Pb concentrations were determined with inductively coupled plasma sector-field mass spectrometry (ICP-SF-MS; Element 2, Thermo Scientific) that allows quantification of trace elements at low ppt levels. Pb concentrations peaked in the 1970s-1980s during the SU economy peak mainly from the use of Pb additives in gasoline and strongly declined in the end of 1980s/beginning of 1990s as the SU collapsed (Fig. 1). The Pb concentration record during 1710-1990 is in exceptional good correspondence with an existing record from the Belukha ice core (Siberian Altai) [3], ~350 km northwest of the Tsambagarav site. Furthermore, the Pb trend agrees well with Pb expert emission estimates for the FSU from the 1950-s until the 1990-s [3]. This is different for the period 1990-2009, where Tsambagarav Pb is increasing, but expert estimates show a decreasing trend, mainly related to the nationwide leaded gasoline ban in Russia in 2003 [4].

To investigate, whether the recent Pb increase is caused by anthropogenic Pb emissions, (a) crustal enrichment factors (EF) of Pb and (b) excess-Pb were calculated following (a) $EF(Pb) = [Pb/Ce]_{\text{sample}}/[Pb/Ce]_{\text{pre-ind.}}$ and (b) $[exPb] = [Pb] - [Pb/Ce]_{\text{pre-ind.}} \cdot [Ce]$ (Fig. 2). Ce was used as a dust tracer, showing the highest correlation with Pb in the pre-industrial period 1710-1760. The trend in exPb at both Altaian sites is in agreement with that of the Pb concentration records. In contrast, trends in calculated Pb EFs disagree between the two sites and are different from those of the Pb concentrations. Thus, a potential error might have been introduced by the calculation of EFs using the Ce records and a critical review of the methods used for dust correction is needed.

An updated Pb record covering the period 1990-2018 from a new Belukha ice core will additionally help to reconstruct the trend in recent FSU Pb emissions.

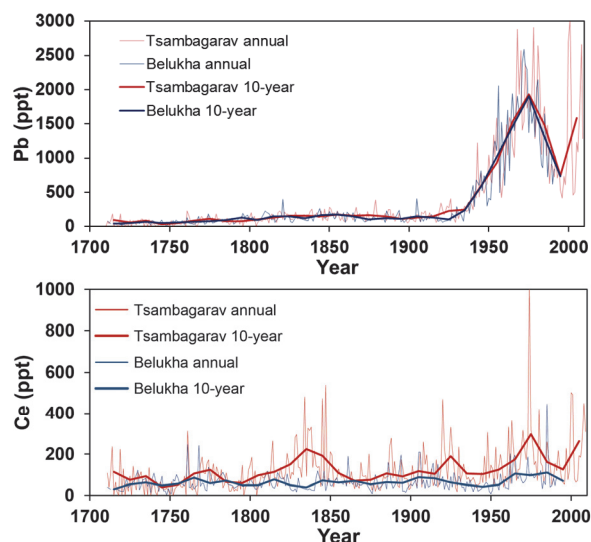


Fig. 1: Annual and 10-year concentration records of Pb (top) and Ce (bottom) from the Belukha and Tsambagarav ice cores.

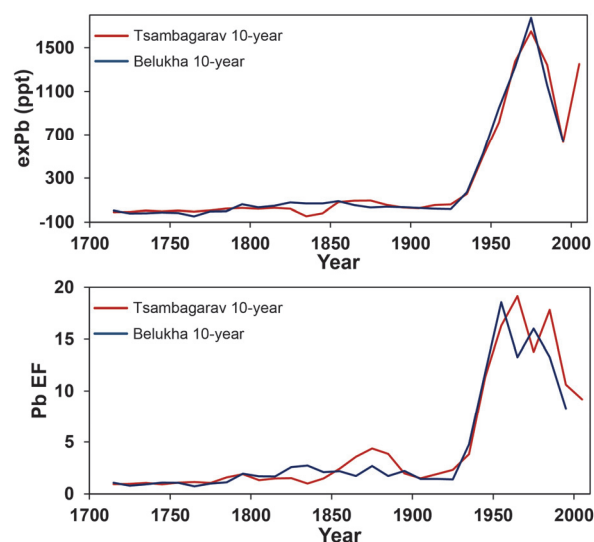


Fig. 2: 10-year mean concentrations of exPb (top) and Pb enrichment factors (EF; bottom) from the Belukha and Tsambagarav ice cores.

We acknowledge funding from the Swiss National Science Foundation (Grant 181985).

- [1] P. Nalivaika et al., LUC Annual Report, **2019**, 30 (2020).
- [2] P. Nalivaika et al., this report, pp. 32
- [3] A. Eichler, et al., Environ. Sci. Technol, **46**, 4323 (2012).
- [4] HELCOM, www.helcom.fi/.

LIST OF PUBLICATIONS

SURFACE CHEMISTRY

- A. Boucly, E. Fabbri, L. Artiglia, X. Cheng, D. Pergolesi, M. Ammann, T. J. Schmidt
Surface segregation acts as surface engineering for the oxygen evolution reaction on perovskite oxides in alkaline media
Chemistry of Materials. 2020; **32**, 5256-5263, doi: 10.1021/acs.chemmater.0c01396
- R. A. Cox, M. Ammann, J. N. Crowley, H. Herrmann, M. E. Jenkin, V. F. McNeill, A. Mellouki, J. Troe, T. J. Wallington
Evaluated kinetic and photochemical data for atmospheric chemistry: volume VII - Criegee intermediates
Atmospheric Chemistry and Physics. 2020; **20**, 13497-13519, doi: 10.5194/acp-20-13497-2020
- J. Edebeli, J. C. Trachsel, S. E. Avak, M. Ammann, M. Schneebeli, A. Eichler, T. Bartels-Rausch
Snow heterogeneous reactivity of bromide with ozone lost during snow metamorphism
Atmospheric Chemistry and Physics. 2020; **20**(21), 13443-13454, doi: 10.5194/acp-20-13443-2020
- J.-D. Förster, C. Gurk, M. Lamneck, H. Tong, F. Ditas, S. S. Steimer, P. A. Alpert, M. Ammann, J. Raabe, M. Weigand, B. Watts, U. Pöschl, M. O. Andreae, C. Pöhlker
MIMiX: a multipurpose in situ microreactor system for X-ray microspectroscopy to mimic atmospheric aerosol processing
Atmospheric Measurement Techniques. 2020; **13**(7), 3717-3729, doi: 10.5194/amt-13-3717-2020
- I. Gladich, S. Chen, M. Vazdar, A. Boucly, H. Yang, M. Ammann, L. Artiglia
Surface propensity of aqueous atmospheric bromine at the liquid-gas interface
Journal of Physical Chemistry Letters. 2020; **11**(9), 3422-3429, doi: 10.1021/acs.jpcllett.0c00633
- M. Kato, R. Nakahoshiha, K. Ogura, S. Tokuda, S. Yasuda, K. Higashi, T. Uruga, Y. Uemura, I. Yagi
Electronic effects of nitrogen atoms of supports on Pt-Ni rhombic dodecahedral nanoframes for oxygen reduction
ACS Applied Energy Materials. 2020; **3**(7), 6768-6774, doi: 10.1021/acsaem.0c00903
- D. Kido, Y. Uemura, Y. Wakisaka, H. Ariga-Miwa, S. Takakuasgi, K. Asakura
Thorough search analysis of extended X-ray absorption fine structure data for complex molecules and nanomaterials applications
e-Journal of Surface Science and Nanotechnology. 2020; **18**, 249-261, doi: 10.1380/EJSSNT.2020.249
- D. A. Knopf, P. A. Alpert, A. Zipori, N. Reicher, Y. Rudich
Stochastic nucleation processes and substrate abundance explain time-dependent freezing in supercooled droplets
npj Climate and Atmospheric Science. 2020; **3**, 2 (9 pp.), doi: 10.1038/s41612-020-0106-4
- X. Kong, D. Castarède, A. Boucly, L. Artiglia, M. Ammann, T. Bartels-Rausch, E. S. Thomson, J. B. C. Pettersson
Reversibly physisorbed and chemisorbed water on carboxylic salt surfaces under atmospheric conditions
Journal of Physical Chemistry C. 2020; **124**(9), 5263-5269, doi: 10.1021/acs.jpcc.0c00319
- K. Maeda, Y. Uemura, W.-J. Chun, S. S. Satter, K. Nakajima, Y. Manaka, K. Motokura
Controllable factors of supported Ir complex catalysis for aromatic C-H borylation
ACS Catalysis. 2020; **10**(24), 14552-14559, doi: 10.1021/acscatal.0c03734
- F. Mahrt, P. A. Alpert, J. Dou, P. Grönquist, P. Corral Arroyo, M. Ammann, U. Lohmann, Z. A. Kanji
Aging induced changes in ice nucleation activity of combustion aerosol as determined by near edge X-ray absorption fine structure (NEXAFS) spectroscopy
Environmental Science: Processes and Impacts. 2020; **22**(4), 895-907, doi: 10.1039/C9EM00525K
- Z. Novotny, D. Aegerter, N. Comini, B. Tobler, L. Artiglia, U. Maier, T. Moehl, E. Fabbri, T. Huthwelker, T. J. Schmidt, M. Ammann, J. A. van Bokhoven, J. Raabe, J. Osterwalder
Probing the solid-liquid interface with tender x rays: a new ambient-pressure x-ray photoelectron spectroscopy end-station at the Swiss Light Source
Review of Scientific Instruments. 2020; **91**(2), 023103 (10 pp.), doi: 10.1063/1.5128600
- Y. Uemura, T. Yokoyama, T. Katayama, S. Nozawa, K. Asakura
Tracking the local structure change during the photoabsorption processes of photocatalysts by the ultrafast pump-probe XAFS method
Applied Sciences. 2020; **10**(21), 1-15, doi: 10.3390/app10217818

ANALYTICAL CHEMISTRY

M. Barandun, J. Fiddes, M. Scherler, T. Mathys, T. Saks, D. Petrakov, M. Hoelzle
The state and future of the cryosphere in Central Asia
 Water Security. 2020; **11**, 100072 (14 pp.), doi: 10.1016/j.wasec.2020.100072

P. Bohleber, M. Schwikowski, M. Stocker-Waldhuber, L. Fang, A. Fischer
New glacier evidence for ice-free summits during the life of the Tyrolean Iceman
 Scientific Reports. 2020; **10**, 20513, 2020, doi: 10.1038/s41598-020-77518-9

A. Eichler, T. Kellerhals, M. Schwikowski
Kupferspuren im Gletscher
 Nachrichten aus der Chemie. 2020; **68**(5), 73-75, doi: 10.1002/nadc.20204095028

L. Fang, S. H. Lee, S.-A. Lee, D. Hahm, G. Kim, E. R. M. Druffel, J. Hwang
Removal of refractory dissolved organic carbon in the Amundsen Sea, Antarctica
 Scientific Reports. 2020; **10**(1), 1213 (8 pp.), doi: 10.1038/s41598-020-57870-6

M. Feltracco, E. Barbaro, A. Spolaor, M. Vecchiato, A. Callegaro, F. Burgay, M. Vardè, N. Maffezzoli, F. Dallo, F. Scoto, R. Zangrando, C. Barbante, A. Gambaro
Year-round measurements of size-segregated low molecular weight organic acids in Arctic aerosol
 Science of the Total Environment. 2020; 142954 (10 pp.), doi: 10.1016/j.scitotenv.2020.142954

J. Guntern, A. Eichler, F. Hagedorn, L. Pellissier, M. Schwikowski, O. Seehausen, C. Stamm, M. van Heijden, P. Waldner, I. Widmer, F. Altermatt
Übermäßige Stickstoff- und Phosphoreinträge schädigen Biodiversität, Wald und Gewässer
 Bern: Akademie der Naturwissenschaften Schweiz (SCNAT). 2020; doi: 10.5281/zenodo.4269631

H. W. Gäggeler, L. Tobler, M. Schwikowski, T. M. Jenk
Application of the radionuclide ²¹⁰Pb in glaciology – an overview,
 Journal of Glaciology. 2020; **66**(257), 447-456, doi: 10.1017/jog.2020.19

G. Jouvét, S. Röllin, H. Sahli, J. Corcho, L. Gnägi, L. Compagno, D. Sidler, M. Schwikowski, A. Bauder, M. Funk
Dating the ice of Gailigletscher, Switzerland, based on surface radionuclide contamination and ice flow modeling
 The Cryosphere. 2020; **14**, 4233-4251, doi: 10.5194/tc-14-4233-2020

S. D. Kaspari, D. Pittenger, T. M. Jenk, U. Morgenstern, M. Schwikowski, N. Buenning, L. Stott
Twentieth century black carbon and dust deposition on South Cascade Glacier, Washington State, USA as reconstructed from a 158 m long ice core
 J. Geophys. Res. Atmospheres. 2020; **125**, e2019JD031126, doi: 10.1029/2019JD031126

M. Kronenberg, H. Machguth, A. Eichler, M. Schwikowski, M. Hoelzle
Comparison of historical and recent accumulation rates on Abramov Glacier, Pamir Alay
 Journal of Glaciology. 2020; **67**(262), 253-268, doi: 10.1017/jog.2020.103

D. Osmont, S. Brugger, A. Gilgen, H. Weber, M. Sigl, R. L. Modini, C. Schwörer, W. Tinner, W. Wunderle, M. Schwikowski
Tracing devastating fires in Portugal to a snow archive in the Swiss Alps: a case study
 The Cryosphere. 2020; **14**, 3731-3745, doi: 10.5194/tc-14-3731-2020

H. Pang, S. Hou, Z. Zhang, S. Wu, T. M. Jenk, M. Schwikowski, J. Jouzel
Temperature trends in the northwestern Tibetan Plateau constrained by ice core water isotopes over the past 7,000 years,
 J. Geophys. Res. Atmospheres. 2020; **125**, e2020JD032560, doi: 10.1029/2020JD032560

AFFILIATION INDEX

ÅAU	Åbo Akademi University, Tuomiokirkontori 3, 20500 Turku, Finland
Areaphoto	Areaphoto Image & Communication, Via Nevegal 71, 32100 Belluno, Italy
CECs	Centro de Estudios Científicos, Arturo Prat 514, Valdivia, Chile
CEA Saclay	CEA Paris-Saclay, 91191 Gif-sur-Yvette, France
CNR-ISP	Istituto di Scienze Polari, Ca' Foscari University Venice, Via Torino, 155, 30172 Venice, Italy
CNRS	Centre national de la recherche scientifique, 3 Rue Michel Ange, 75016 Paris, France
Dolomiti Guides	Guide Alpine Dolomiti Guides, Via Rivinal, 95/c, 32100 Belluno, Italy
ENE	Energy and Environment, Paul Scherrer Institut, 5232 Villigen, Switzerland
ETHZ	ETH Zürich, Eidgenössische Technische Hochschule Zürich, 8092 Zürich, Switzerland
FUGA	Fondation Université Grenoble Alpes, 621 Avenue Centrale, 38400 Saint-Martin-d'Hères, France
IPEV	Institut Polaire Français Paul-Émile Victor, Zoning Industriel Pointe du Diable, 29280 Plouzané, France
IRD/IGE	Institut de Recherche pour le Développement/Institut de Géosciences de l'Environnement, UGA – IGE, 38058 Grenoble Cedex 9, France
IWEP	Institute for Water and Environmental Problems, Ulitsa Molodezhnaya, 1, Barnaul 656038, Altai Krai, Russia
LBK	Bioenergy and Catalysis Laboratory, Paul Scherrer Institut, 5232 Villigen, Switzerland
LEC	Laboratory for Electrochemistry, Paul Scherrer Institut, 5232 Villigen, Switzerland
LMN	Laboratory for Micro and Nanotechnology, Paul Scherrer Institut, 5232 Villigen, Switzerland
LMX	Laboratory for Multiscale Materials Experiments, Paul Scherrer Institut, 5232 Villigen, Switzerland
LSC	Laboratory for Condensed Matter, Paul Scherrer Institut, 5232 Villigen, Switzerland
LSK	Laboratory for Catalysis and Sustainable Chemistry, Paul Scherrer Institut, 5232 Villigen, Switzerland
LUC	Laboratory of Environmental Chemistry, Paul Scherrer Institut, 5232 Villigen, Switzerland
MPIC	Max-Planck-Institut für Chemie, Hahn-Meitner-Weg 1, 55128 Mainz, Germany
NES	Nuclear Energy and Safety Division, Paul Scherrer Institut, 5232 Villigen, Switzerland
PSD	Photon Science Division, Paul Scherrer Institut, 5232 Villigen, Switzerland
PSI	Paul Scherrer Institut, Forschungsstrasse 111, 5232 Villigen, Switzerland
QEERI	Hamad Bin Khalifa University, Qatar Environment and Energy Research Institute, Education City, Doha, Qatar
SLB	SLB-analys, Fleminggatan 4, 104 20 Stockholm, Sweden
SMHI	Swedish Meteorological and Hydrological Institute, 601 76 Norrköping, Sweden
THU	Tsinghua University, Haidian District, Beijing, 100084, China
TROPOS	Leibniz-Institut für Troposphärenforschung, Permoserstrasse 15, 04318 Leipzig, Germany
UBC	The University of British Columbia, Vancouver Campus, 2329 West Mall, Vancouver V6T 1Z4, Canada
UGA	Université Grenoble Alpes, 621 Avenue Centrale, 38400 Saint-Martin-d'Hères, France
Univ. Bern	Universität Bern, Departement für Chemie, Biochemie und Pharmazie, Freiestrasse 3, 3012 Bern, Switzerland
Univ. Chile	Universidad Austral de Chile, Independencia 631, Valdivia, Chile
Univ. Colorado	University of Colorado Boulder, Department of Chemistry, 215 UCB, and Cooperate Institute for Research in Environmental Sciences (CIRES), Ekeley Sciences, 216 UCB, Boulder, CO 80309, USA
Univ. Fribourg	Université de Fribourg, Avenue de l'Europe 20, 1700 Fribourg, Switzerland
Univ. Gothenborg	The University of Gothenburg, Universitetsplatsen 1, 405 30 Gothenburg, Sweden
Univ. Leeds	University of Leeds, Leeds, LS2 9JT, United Kingdom
Univ. Lille	Université de Lille, 42, rue Paul Duez, 59000 Lille, France
Univ. Venice	Ca' Foscari University, Dorsoduro 3246, 30123 Venezia, Italy
Xiamen Univ.	Xiamen University, No. 422, Siming South Road, Xiamen, Fujian, 361005, China

Paul Scherrer Institut :: 5232 Villigen PSI :: Switzerland :: Tel. +41 56 310 21 11 :: www.psi.ch

